Testing the influence of laser pulse energy and rate in the atom probe tomography analysis of minerals

Chiara CAPPELLI[1,*,#] and Alberto PÉREZ-HUERTA[1]

[1]*Department of Geological Sciences, The University of Alabama, Tuscaloosa, AL 35487, USA*

*Corresponding author – E-mail: ccappelli@ua.edu, ccappelli@ub.edu

Present address: MAiMA group, Department of Mineralogy, Petrology and Applied Geology, University of Barcelona (UB), Martí Franquès s/n, 08028 Barcelona, Spain

Abstract

The use of atom probe tomography (APT) for mineral analysis is contributing to fundamental studies in Earth Sciences. Meanwhile, the need for standardization of this technique is becoming evident. Pending the use of mineral standards, the optimization of analysis parameters is needed to facilitate the study of different mineral groups in terms of data collection and quality. Laser pulse is one of the variables that highly affects the atom evaporation process occurring during APT analysis and its testing is important to forecast mineral behavior and obtain the best possible data. In this study, five minerals representative of major groups (albite, As-pyrite, barite, olivine, monazite), were analyzed over a range of laser pulse energies (10-50 pJ) and rates (100-250 kHz) to assess output parameter quality and evaluate compositional estimate stoichiometry. Among the studied minerals, As-pyrite, ~~whit~~ with the higher thermal conductivity and lower band gap, was the most affected by the laser pulse variation. Chemical composition estimates equal or close to the general chemical formula were achieved for monazite and As-pyrite~~, and albite~~. The analysis of multihit events has proved to be the best strategy to verify the efficacy of the evaporation process and to evaluate the best laser pulse setting for minerals.

Key words: laser pulse, experimental parameters, background level, mass resolution, multihit~~ple~~ events, stoichiometry

Introduction

Geoscience is increasingly benefiting from the application of the atom probe tomography (APT) to the study of minerals (e.g., Daly et al., 2021; Gamal El Dien, 2021; Gopon et al., 2021; Joseph et al., 2021; Lee et al., 2021; Taylor et al., 2021). Even though the chemical and spatial information gathered by APT places this technique among the best tools for atomic resolution analysis of minerals, the intrinsic variability of the analyzed specimens prevents, in general, the use of reference materials for instrument calibration and data correction (Reddy et al., 2020). APT is a "sample-based" microscopy technique, sensitive to the needle-shape geometry due to the instrument set-up and the nature of the physical processes involved in the specimen analysis. Hence, the standardization of APT mineral analysis is extremely difficult since no specimen is equal to another. At the same time, suggestions for common practices of data reporting and analysis routines have been proposed (Blum et al., 2018; Exertier et al., 2018; Fougerouse et al., 2021; Saxey et al., 2018a) and indicative ranges for parameter settings have been defined for some minerals (Joseph et al., 2021; La Fontaine et al., 2017; Verberne et al., 2019).

Laser pulse energy (PE) and laser pulse rate (PR) are among the variables that have a major effect in both the spatial and compositional ~~APT~~ characterization of minerals by laser-assisted APT. The physical principle of the APT consists in the evaporation of atoms from a needle-shaped specimen and their immediate ionization (Kelly, et al., 2014; Silaeva, et al., 2013; Vurpillot, et al., 2009). These processes are enabled by the application of an intense electric field and highly energetic laser pulses (in the case of laser-assisted evaporation) to the specimen. Both the PE and PR, together with other system conditions (e.g., detection rate, temperature, pressure) and the sample geometry (often material dependent), determine the rate and yield of the evaporation process. In general, the increase of PE decreases the field-induced stress improving the yield (Kelly

& Larson, 2012), while high PR (frequency of the laser pulse) allows larger amounts of evaporated atoms per unit time (Prosa, et al., 2019). Despite these general criteria, in order to perform a succesful analysis, t~~T~~he choice of the~~se~~ laser parameters is key to minimize artifacts (i.e., trajectory aberrations) and other biases that arise due to phenomena associated to the laser-specimen interaction (Cappelli et al., 2021b), mostly related to the overheating of the tip specimen and/or the overlapping of evaporation events. Sample-specific adjustments of the laser setting are~~is~~ then fundamental for reliable results and the investigation of the best parameter conditions for a group of minerals is paramount to promote the routinely employment of APT in geosciences.

Despite the specimen-specific nature of the APT analysis, common behavior, i.e., analysis outcome, is expected for minerals of the same group, similar composition and/or similar optical and thermal properties. Oxides for example may be affected by a deficit of oxygen due to the formation of neutral species that remain undetected (Devaraj, et al., 2013, Gault et al., 2016). Silicates may suffer oxygen and silicon loss-in-detection for the ion pile-up phenomenon and/or molecular species dissociation (Cappelli et al., 2021). The presence of light elements or elements with strongly different field evaporation values in the structure of a mineral induce ion preferential evaporation and migration over the tip surface (Vurpillot & Oberdorfer, 2015). In addition to these general considerations, a specific interaction between the mineral and the applied laser pulse would depend on the mineral properties and the characteristics of the laser (e.g., Lu, et al., 2017; Santhanagopalan, et al., 2015). Laser adsorption depth and thermal conductivity and diffusivity of a material will determine the heat dissipation between laser pulses during an APT analysis (Valderrama et al., 2015).

In the present study, five minerals have been selected to test the influence of laser pulse energy and rate, in the range 10-50 pJ and 100-250 kHz, respectively. Three output variables,

65 background, mass resolution, and the amount of multiple hits, have been analyzed and, for each
66 mineral, the composition estimates obtained for each specific set of experimental conditions have
67 been compared. The five minerals chosen are representative of different classes/groups: olivine
68 and albite for neso and tectosilicate respectively, the sulfide arsenopyrite and the sulphate barite,
69 and the cerium/lanthanum phosphate monazite. Each of these minerals have relevance for
70 geological studies, and a summary is provided as follows:

71 - Olivine, with general formula $(Mg,Fe)_2SiO_4$, is an important rock-forming mineral and is
72 common in mafic and ultra-mafic igneous rocks (Alderton 2021). Feldspars are the most abundant
73 mineral group in Earth crust and albite (general formula $NaAlSi_3O_8$) lies between the two main
74 feldspar compositional series, that is alkali feldspars and the plagioclase series (Brown et al.,
75 2006). Both, olivine and albite properties have been investigated to understand the physical state
76 of the interior of the Earth (Alderton, 2021; Suzuki et al., 2002). Olivine is also important for its
77 presence on the lunar surface and in meteorites (Krot et al., 2014), while replacement reactions
78 leading to albite formation from alkali and plagioclase feldspars is a studied common process
79 occurring in the Earth's upper crust (albitization phenomenon) (Hövelmann et al., 2010).
80 - Barite ($BaSO_4$) is a common sulphate mineral found in sedimentary environments and its
81 formation in different geological settings makes it useful for paleoenvironmental, hydrogeological,
82 and hydrothermal investigation (e.g., barite isotope studies for records of subseafloor processes)
83 (Griffith & Paytan, 2012). Sulphates are important in industry and, in particular, barite has been
84 used as additive in drilling mud, although its use expands from pigmentation in paints to diagnostic
85 medical tests (for its property of shielding X~~x~~-ray emissions).
86 - Arsenopyrite (or As-pyrite, general formula AsFeS), found in a large range of ore deposits, is
87 often mined and processed to extract the associated gold. The oxidation of the arsenopyrite-

enriched waste from mining releases S and As. The waters of Au acidic mine drainage have then often high concentration of As, a highly hazardous element for the environment and the public health (Corkhill & Vaughan, 2009). Besides the interest on As-pyrite oxidation, this mineral is also studied for its utility in geothermometry (Vaughan, 2021).

- Monazite, a light rare-earth element phosphate (the most common Ce-monazite, $(Ce,La,Nd,Th)PO_4$), is an important accessory mineral of granites that concentrates in alluvial sands after being released by the weathering of pegmatites (Clavier et al., 2011; Rapp & Watson, 1986). Among its uses, maybe the most studied in geoscience is the application in geochronology for the significant amount of U and Th in the mineral.

Methodology

Sample preparation and instrumental settings

The five minerals used in this study have been purchased from SPI Natural Mineral Group as single crystals. The specimens for atom probe analysis were prepared following a conventional focused ion beam (FIB) protocol (Gault et al., 2012; Larson et al., 2013; Miller & Forbes, 2014), using a dual beam scanning electron microscope (TESCAN LYRA FIB-FESEM) after a sample gold coating of ~ 20 nm for minimizing surface charging effects. Specifics on the acquisition conditions and the specimen geometry can be found in the Supplementary Information (SI) 1.

Two specimens for each mineral were analyzed in laser mode (laser wavelength of 355 nm) by a local electrode atom probe (LEAP 5000 XS, housed at the AARC of The University of Alabama) for testing the laser pulse energy (PE) and pulse rate (PR), respectively. The pulse energy was varied every 4-6 M ions from 50 to 10 pJ and ~3 to 5 M ions were sampled for the reconstruction of the specimen at each PE condition (see Fig. 1). Similarly, the pulse rate varied

from 100 to 250 kHz and a sampling of 3-5M ions was performed to generate data sets for each condition. The detection rate was fixed for all the runs at 0.5% while the pulse rate for the PE testing was set at 125 kHz and the pulse energy for the PR testing was kept at 50 pJ. Note that values with low PE (10-50 pJ) and PR (100-250 kHz) ranges were chosen in the present study to minimize issues related to the slow heat dissipation of insulator materials. A replica (specimen 2 taken from the same wedge of specimen 1) for the PE effect on barite and albite APT analysis was performed and an additional specimen for the PR testing of As-pyrite was analyzed at PE of 20 pJ (see SI 1). In all the runs, the direct current (DC) voltage varied freely to maintain a stable detection rate.

<Figure 1 here>

Integrated Visualization and Analysis Software (IVAS 3.8.10) from CAMECA was used for the data sets processing. Ion species were defined for each peak of the APT spectra fixing the peak range to a width of 0.1 Da for the lower bound and 0.2 Da for the upper bound to account for possible peak tails. Exceptionally, when bigger tails were observed, the ranges were manually broadened without interfering with contiguous peaks. Overlap of contiguous peaks was resolved by the decomposition tool, used in each run for the estimate of the mineral chemical composition. Note that, when present, the peak at 16Da was only assigned to $16O^+$, as already justified in a previous work (Cappelli et al., 2021b).

Output parameters

The effect of laser pulse energy and rate has been studied by analyzing the variation of three main variables: background, resolution, and multiple hits. The considered resolution was the ~~mass resolution~~mass resolving power ($M/\Delta M$) (mass resolution hereafter), where M stands for the

mass of the highest peak in the spectrum and ΔM for the full width at half maximum (see SI 1). The background values were compiled from the IVAS reconstruction. The background model is in this case Global ToF-based (estimated on the entire dataset). Note though that the background default model implemented during the decomposition of the mass spectra was the local range-assisted. The multi hit percentage for each run and experimental condition was calculated from IVAS EPOS files using a MATLAB R2020a script.

Results

Analysis of the output variables

The variation of the three considered variables has common tendency among the analyzed minerals and substantial differences in some cases (Fig. 2).

<Figure 2 here>

The IVAS-calculated background decreases with the increase of PE (Fig. 2a) and the decrease of PR (Fig. 2b), with barite and albite showing the higher variability. Similarly, the mass resolution decreases in general at higher pulse energies and lower pulse rates, although As-pyrite show a clear maximum at 30 pJ (Fig. 2b) and no improvement was observed at laser energy values <20pJ (Fig. 2c) (i.e., albite and monazite) or rate values >200 kHz (Fig. 2d) (i.e., olivine and As-pyrite). The multiple hits variation over the PE range studied is significant for As-pyrite and albite, showing an increase with the increase of pulse energy (Fig. 2e). On the other hand, when the pulse rate is increased, the percentage of multiple hits is almost constant over the studied range for all the minerals (Fig. 2f). Nevertheless, considering the reproducibility of the multihits tendency of replicated runs (different specimens and same experimental conditions (or similar in the case of

As-pyrite)), the slight variation of this output parameter has been considered reliable for further data analysis (see "Charge state ratio vs multihits" section in the Discussions).

Compositional estimates

APT compositional estimates of the studied minerals are shown in the SI 2, whereas this section is focused on the analysis of the elemental stoichiometric ratios of each studied mineral (Figs. 3 and 4).

As documented in previous APT studies on different minerals (Bachhav et al., 2013; Cappelli et al., 2021a; Cappelli et al., 2021b; Fougerouse et al., 2018; Gordon et al., 2012; Kinno et al., 2014; Santhanagopalan et al., 2015), the oxygen-containing minerals are affected by a general deficit of oxygen (Figs. 3 and 4c,d), with the exception of monazite (Fig. 4a,b). In the latter case, although the ratio (Ce+La)/O is lower than the stoichiometric value, both P/O and REEs/O gave values near to the stoichiometry over the entire range of laser pulse and rate explored, with the composition recorded for the initial conditions of PE 50 pJ, PR 250 kHz and DR 0.5% matching the mineral stoichiometry. ~~Interestingly, despite the loss of O and the deficit of Na (especially for specimen 2 of the PE testing and the PR testing) of albite composition (Fig. 3a,b), the elemental ratios are quite close to the stoichiometry, with an absolute difference between the nominal and the calculated values ≤0.07 and ≤0.05 for the Si/O and Al/O ratios, respectively, over the entire experimental range, and ≤ 0.06 for the Na/O ratios of the specimen 1 of the PE testing.~~

The excess of Al measured for albite remarks the loss of O as well as Si and Na (Fig. 3a,b). The absence of the Si/O ratio stoichiometry denotes high O undetected counts, with the calculated *versus* nominal ratio difference ranging between 15 to 19%, which means that the deficit is not

necessarily related to Si_xO_y species. A general deficit of Na was observed especially for the specimen 2 (replica) of the PE-testing and the PR-testing specimen.

As for olivine, ~~A~~an excess of Mg+Fe ~~in olivine~~ throughout the PE and PR applied ranges reveals the probable loss of Si together with O since the ratio Si/O is closer to the stoichiometric value (Fig. 3c,d). A similar pattern is shown for barite (Fig. 4c,d), which Ba amount is much higher than both O and S (i.e., S/O closer to the stoichiometry than Ba/O) and it seems to decrease with PR increase and PE decrease. Note that the excess of S with respect to O may be due to the difficulty in resolving the overlap of the S^+ and O_2^+ peaks in the range 32-36 Da. Indeed, IVAS decomposition tool was not able to perform a proper peak assignation, undercounting oxygen ions. However, it is difficult to assess if the observed oxygen deficit is only due to a poor deconvolution or also to phenomena leading to ion lack-of-detection (e.g., neutrals formation).

As-pyrite appears to be greatly sensitive to both laser pulse energy and rate (Fig. 4e,f and Fig. SI3-2 in SI 3). The ratio As/S is quite variable although always lower than the stoichiometric value. The ratio Fe/S seems to decrease with the PR increasing, starting from higher than stoichiometric value at 100 kHz and falling to near stoichiometry (PR 250 kHz, 50pJ). The analysis conditions that gave the better outcome are PE 30 pJ, PR 125 kHz and DR 0.5% (see black circle in Fig. 4e), with a As/S ratio that differs ≈0.07 from the nominal value.

<Figure 3 here>

<Figure 4 here>

Discussions

Quality of output parameters

The three output parameters analyzed in the present study (background, mass resolution, and multihits) do not vary significantly over the experimental conditions. Considering the small ranges obtained for each variable, it is difficult to derive definitive conclusions. Nevertheless, the reproducibility of the few replicas performed (Fig. 2) gives some space for discussion of results, without falling in speculative arguments.

A trend for each variable and mineral may be recognized. The first observation ~~on this regard~~ concerns the background *versus* mass resolution trends (Figs. 2a-d). The decrease of the background with the laser energy should induce an improvement (increase) of the mass resolution. This was not the case for the trends of the recorded data. To verify the reliability of the Global ToF-based background values retrieved from the IVAS software reconstructions, a baseline for each mass spectrum was measured by OriginPro-2020 software. Each spectrum was normalized to the maximum peak and the median was taken as a reference for the baseline. Opposite tendencies with respect to the IVAS background were reveled when the baseline values were plotted against the laser energy and rate (Fig. 5). In general, the highest values were measured at 50 pJ laser energy and 100 kHz laser rate, except for the As-pyrite (Fig. 5a). The increase of the global (ToF-based) background with the laser energy decrease and the pulse rate increase may be an artiefact related to the presence of several overlapping peaks and a variable background level in complex ~~mass~~ spectra (Exertier, et al., 2018). ~~For example, the wide ToF range of barite leads to variations across the entire range of the mass spectrum, with a notable difference between the background level up to ~64 Da and after this value (Fig. SI4-1 in SI 4)~~.

<Figure 5 here>

Most minerals are good insulator materials and, despite the efficiency of the APT laser pulse in triggering atom evaporation from the needle-shape specimen surface, they are affected by a slow heat dissipation. Higher laser energy means higher heating of the tip and, hence, slower cooling-down between sequential laser pulses, which in turn may induce late evaporation events and the consequential increase of the background and decrease of the mass resolution (i.e., higher thermal tails). As-pyrite, with~~whit~~ higher thermal conductivity and lower optical band gap compa~~e~~ering with the other minerals analyzed (Table 1), is ~~apparently less~~ differently affected by the laser energy increase (Fig. 5a). An even evaporation of the ion species and a lower probability of direct current (DC) (i.e., field-induced) evaporation events may be the cause of the baseline *versus* laser energy trend of As-pyrite, since the higher the laser energy the lower the electric field needed for the field evaporation of surface atoms at a specific detection rate. The maximum mass resolution observed at 30 pJ was confirmed by the calculation of the (M/ΔM) based on the local FWHM of the $^{28}Fe^{2+}$ peak (OriginPro-2020 measurements; Fig. SI4-2 in SI 4) and corresponds to the value giving the composition estimate closest to the nominal. ~~The As-pyrite heat dissipation probably worsens for laser pulse energy values >30pJ.~~ This must be related to the percentage of multihit events which increased with the laser pulse energy increase (Fig. 2e; see also next section).

<Table 1 here>

On the other hand, the general increase of the mass resolution with the laser pulse rate suggests that smaller windows between laser pulses (i.e., higher pulse rates) improve the ion species differentiation, up to PR values where the tip cooling is prevented. Although high laser pulse rate may induce late evaporation events, it also helps to avoid thermal gradients and the

possible generation of ion diffusion on the tip surface yielding to a more even evaporation of the ionic species (Kirchhofer et al., 2013; Riley et al., 2012).

The different behavior of As-pyrite during APT analysis with respect to more insulator minerals suggests that a careful study of the microscopic properties of a mineral may help define an appropriate range of experimental conditions. A multivariable regression analysis performed by MATLAB R2020a reveals for example a good correlation between the thermal conductivity of the minerals, the baseline and mass resolution values and the laser pulse energy and rate used in the present study (see SI 5). Similar investigation on a wider data range could be useful to identify the experimental conditions for the APT analysis of a mineral knowing its thermal properties.

Also, the comparison of the obtained results with previous reported data (Table 2) demonstrates the importance of classifying data sets by instrument system. Different combination of experimental parameters, including detection rate or temperature, may prompt a different response of the atoms/molecules during evaporation from the specimen surface and improve/change the actual detection efficiency of an APT analysis. However, the results obtained in this study by a LEAP 5000 XS are in fact not wholly comparable with data gathered by previous generation or reflectron-equipped instruments.

<Table 2 here>

Charge state ratio vs. multihits

The laser pulse energy, in the studied range, particularly affects the multiple hits events percentage of As-pyrite, while the effect on the other minerals is low. A slight effect of the PR on the multi-hits amount is in general apparent and the variation with the pulse rate is not consistent between minerals. Multiple events should depend on the strength of the electric field and, in

general, multihits count increases at higher surface electric field (Müller et al., 2012; Saxey et al., 2018b; Verberne et al., 2019). Therefore, for a better analysis of the multiple hit events incidence, their dependence on the surface electrical field was considered using the charge state ratio (CSR) of the main ion species as field proxy (Fig. 6), except for barite with a~~hose~~ spectra that do not display single and double ionized species of the same element. Note that, Al ratio has been chosen for albite and olivine because the small peak of Mg^{+} (sensitive to the ranging) and the possible interference of Fe^{2+} with Si^{+} peaks make these elements not representative. Also, only one specimen for albite was considered (specimen 1 with the more reliable composition; see next section). On the contrary, La and Fe are well representative of monazite and As-pyrite, respectively. Despite the little variability of multiple events over the studied ranges of laser pulse energy and rate, interesting trends were found, and some important considerations can be made for each mineral. In this regard, it is worth noting that the multihits range of olivine and monazite is particularly narrow and the following discussion is only an attempt to describe the potential utility of the CSR and oxygen ion fraction (O-IF) combined study. Further investigation on wider PE and PR ranges is needed to verify the information reported in the present study about the variability of these two parameters.

Albite. The amount of multi-hits consistently decreases with the Al charge state ratio increasing (Fig. 6a,b). Multiple events should be triggered by higher surface electric field (i.e., higher CSR). The unexpected behavior of albite may depend on the effect of the field on the stability of molecular species. Either sympathetic co-evaporation of ion species from the surface or field evaporation and subsequent dissociation of a molecular species may account for multiple hit events (Saxey, 2011). In the latter case, higher field would stabilize metastable parent species preventing their dissociation that~~which~~ conversely is favored at low field conditions (Di Russo et

al., 2017; Saxey, 2011). This implicates that the CSR is not always a reliable proxy for field strength of oxygen-bearing minerals (Cappelli et al, 2021). Despite the latter reasonable considerations, it should be considered that the significant Na (alkali metal) deficit suggests the existence of detrimental processes before or during the specimen analysis (Lu, et al., 2017; Pfeiffer, et al., 2017; Santhanagopalan, et al., 2015; Yoo, et al., 2022), which may also be affecting mutihits counts (early fractured replica of the PE-testing was therefore not included in this discussion). When using the oxygen ionic fraction as a different proxy (Fig. 7a,b; see also next paragraphs), the trend of the PE-testing specimen (Fig. 7a) inverts up to 30 pJ (note that the 50 pJ run corresponds to the top of the tip, i.e., higher possible damage during specimen FIB-preparation). Nevertheless, It is also worth noting that, the CSR decreases with the PE increase, in agreement with the theory (e.g., Gault et al., 2010), and increases with the PR.

Olivine. The multiple event percentage decreases with the Al-CSR increasing up to 20 pJ, experiencing a sudden increase at 10 pJ (Fig. 6c), maybe for a worsening of the field evaporation process at low thermal pulse. The PR plot (Fig. 6d) displays multi-hits and CSR decrease at a value of 250 kHz. The higher pulse rate may either be improving the evaporation process or enhance the loss of ion species which would be reflected on both the multiple event counts and the double ionized Al. A correct assessment is difficult to make since the estimated composition of olivine is quite constant over the studied PR (Fig. 3b). As stated in a previous work (Schreiber et al., 2014), the oxygen ionic fraction (O-IF=$O^+/(O^+ + O^{2+})$) can be also considered a good proxy for the surface electric field and might help in the data interpretation (see Fig. 7). O-IF for olivine (Fig. 7d) increases with the pulse rate. However, low multi-hits are recorded for a value of 250 kHz suggesting an undercounting of multi-hits maybe due to a higher pile-up (i.e., ion falling in the dead time and dead zone detection frame) that would leave part of the ion counts undetected. Near-

in-time events may also be detected as background for the shorter time window at higher pulse rates. The O-IF of the PE plot shows an "anomaly" at 10 pJ (Fig. 7c), similarly to the CSR graph, but the ratio then increases with the pulse energy (contrarily to the CSR trend). The opposite behavior to the theory observed in the range 20-50 pJ has been already documented for example for garnet (Cappelli et al., 2021b) and it may be due to a bias of the relative concentration of single/double ions for the enhancement of oxygen loss as neutral O_2 molecules at higher laser energy.

Monazite. The multiple events increase with the La-CSR over the PE and PR studied ranges (Figs. 6e,f). However, as in the case of olivine, the PR plot (Fig. 6d) displays a decrease of both multi-hits and CSR at a value of 250 kHz but, this time, the multiple events increase with the O-IF (Fig. 7f) as for La-CSR, suggesting that a real improvement of the evaporation process is in place. The stoichiometric ratio measured at the PR value of 250 kHz (Fig. 4b) points to the same conclusion. The similar tendency of the CSR and O-IF vs PE plots is also consistent with the theory and the near to stoichiometry compositional estimate for monazite over the studied ranges.

As-pyrite. A multiple-hits percentage increase with the Fe-CSR in the range of the PE tested is apparent (Fig. ~~6h~~6g) while opposite tendencies for the 20 and 50 pJ runs of the PR testing are reveled (Fig. ~~6i~~6h). Specific elements are preferentially involved in the formation of multiple events because of the large electric field they need to be field evaporated (Peng et al., 2018). Moreover, the nature of the atom bonding of a material and the charge rearrangement on the material surface after the field evaporation of an atom also determine the proportion of the multiple events (Gault et al., 2021). Hence, the same material is expected to behave similarly with the variation of the surface electric field, which contrasts with our observations. The divergent behavior of the multiple hit's dependence on the field from the theory may be due to the lack of

328 detection of double ionized species and/or multihits. This might be affecting the dependence of
329 the multihits on the CSR calculated for the PR testing of As-pyrite at constant pulse energy of
330 50pJ. The CSR decreasing above 100 kHz may be due to the loss of Fe^{2+}, most abundant than Fe^{+}
331 and therefore more prone to undergo ion pile-up. Indeed, according to the compositional estimates,
332 Fe/S ratio decreases with the increase of the PR (although at 250 kHz is near to its stoichiometric
333 ratio) (Fig. 4f, PR (50pJ)). The CSR increasing with the laser pulse energy has been already
334 observed in previous works (Cappelli et al., 2021b; Schreiber et al., 2014; Verberne et al., 2019)
335 and, in the case of As-pyrite, it is most probably due to possible direct evaporation of double
336 ionized species favored at higher laser energy (Schreiber et al., 2014).

337 <Figure 6 here>

338 <Figure 7 here>

339 **APT application for mineral compositional analysis**

340 During APT analysis of minerals, the composition estimates may be biased by phenomena
341 such as ion species preferential retention/evaporation (Devaraj et al., 2017; Felfer et al., 2012), ion
342 migration (Karahka et al., 2015; Yao et al., 2010), and multiple evaporation events and molecular
343 species dissociation (both possibly leading to ion pile up and neutral molecules formation) (Gault
344 et al., 2016; Meisenkothen et al., 2015; Peng et al., 2018; Santhanagopalan et al., 2015; Saxey
345 2011). The setting of a right combination of experimental parameters can avoid or at least minimize
346 the detrimental effects of such processes.

347 The ranges of pulse energy and rate investigated provide estimates that match the nominal
348 monazite composition and are close to the As-pyrite ~~and albite~~ composition, whereas an important
349 deficit of O and ratios far from the stoichiometric values were recorded for albite, barite, and

olivine (Figs. 3 and 4). Previous works on phosphates, sulphates and silicates documented oxygen deficit during APT analysis (Cappelli & Pérez-Huerta, 2020; Cappelli et al., 2021b; Fougerouse et al., 2018; Gordon et al., 2012; La Fontaine et al., 2016; Santhanagopalan et al., 2015; Weber et al., 2016). The propensity to form molecular species with oxygen may be one of the reasons explaining the lack of stoichiometry for these minerals. The prevalent covalent nature of Si-O and S-O bonds may cause the evaporation of molecules which can experience dissociation leading to ion pile-up and/or formation of neutral species (especially O_2^0). Indeed, the near-to-stoichiometry Si/O ratio in olivine and the excess of Mg+Fe is suggesting that ions are lost as molecule species (Si_xO_y). A similar consideration can be made for barite whose estimated composition shows a high excess of Ba. The deficit of Na for albite, on the other hand, may be due to the low evaporation field of this element that could trigger a preferential evaporation and, hence, a count loss for this element. In addition, in the case of the albite PR testing and the replica of the PE testing, the low Na concentration may also be attributed to a FIB damage of the specimen during the lift-out protocol. Both specimens used for the above-mentioned testing underwent a second FIB low-kV cleaning performed to minimize Ga implantation. Therefore, a Na loss due to the intense surface polishing cannot be ruled -out. To explore this possibility, ROIs (regions of interest) of the reconstructions of each tip and condition set were performed over restricted areas (cubes of 10 nm^3) at the center of the tips. The Na loss triggered by the FIB cleaning should be limited to (or higher at) the external part of the tip while the central area should be more preserved. No difference was recorded between the Na/O ratios of the ROIs and the bulk for the PR-testing and PE replica. However, the ROI's values calculated for specimen 1 of the PE-testing were closer to the stoichiometric ratio (although they still do not match stoichiometry). The error between estimated and nominal ratio decreased from 31-46% of the bulk to 24-29% of the ROIs. In addition, a general increase of the Na

concentration was observed along the *z* direction for each tip analyzed (i.e., from 50 to 10 pJ for the PE-testing and from 100 to 250 kHz for the PR-testing, see Supplementary 2). This hints to a detrimental effect of the FIB cleaning that mitigates as the tip radius increases and the weight of the external affected area on the total analyzed volume decreases. A lighter tip FIB-cleaning (using 2 kV), a different tip geometry (radius ≥ 50 nm), longer runs and ROI measurements may be strategies to avoid or minimize the deficit of alkali metal such as Na. Also, the use of a Xe plasma FIB instead of a Ga-FIB might avoid (or minimize) tip damage and Ga interference (Yoo, et al., 2022).

The stoichiometric ratios obtained for monazite suggest that the phosphate group might be more stable after evaporation than the sulphate group or the silicon-oxygen tetrahedron. The data collected during APT analysis show a general higher percentage of P_xO_y and $REEPO_y$ species for monazite than molecular species for olivine (Si_xO_y), albite (Al_xO_y,Si_xO_y) or barite (S_xO_y, $(Ba,La,Ce)_iS_xO_y$) (see SI 3). Previous studies on different phosphates (e.g., bioapatite (Gordon et al., 2012; La Fontaine et al., 2016); $LiFePO_4$ (Santhanagopalan et al., 2015)) documented a deficit of oxygen for the APT compositional estimates. Trivalent REEs in monazite could be stabilizing the evaporating molecular ions whose dissociation is minimized, despite the high electric field.

Correlation histograms (Saxey plots) are a useful tool to investigate the atom evaporation process and explain incongruency in the element concentration estimates. A Saxey plot is based on the ion correlation analysis of the multiple events; it shows graphically the correlation between ion-pairs that evaporates within the same multi-hit event (Saxey, 2011). The comparison between the Saxey plots of the minerals analyzed (Figs. 8 and 9) unveils the main process leading to the element deficit and the lack of stoichiometry of the compositional estimates measured in the present study. In all the correlation histograms, in addition to the coincidence nodes (in yellow)

between ion species corresponding to the major peaks in the mass spectrum, vertical, horizontal, and diagonal trails are apparent revealing the expected late evaporation events (Cappelli, et al.; Santhanagopalan, et al., 2015; Saxey, 2011). Also, dissociation paths of molecular ion species are described by the curve lines connecting nodes to the diagonal.

According to the monazite Saxey plot, cerium phosphate dissociation contributes to the CeO^+ and PO_2^+ peaks following the reaction (Fig. 8a,b):

$$CePO_3^{2+} \rightarrow CeO^+ + PO_2^+$$

The unstable $CePO_2$ molecule recombines in the more stable Ce and P oxide forms. Two more evident dissociation tracks, among other faint ones, in the lower Da range (Fig. SI4-3a in SI 4) can be described as:

1) $PO_2H^{2+} \rightarrow PO^+ + O^+ + (H^0)$

2) $PO_3^{2+} \rightarrow PO^+ + O_2^+$

The reaction 1 discloses the possible formation of hydrogenated species during an APT analysis due to the H contamination of the LEAP reaction chamber.

Dissociation tracks are also visible in the As-pyrite and albite plots (Figs. 8c,d and 9a and Fig. SI4-3b in SI 4) and are described by the following reactions:

As-pyrite

1) $AsS^{2+} \rightarrow As^+ + S^+$

2) $As_2S^{2+} \rightarrow As^+ + AsS^+$

albite

1) $SiO^{2+} \rightarrow Si^{+} + O^{+}$

2) $AlO^{2+} \rightarrow Al^{+} + O^{+}$ $(faint)$

3) $SiO_2^{2+} \rightarrow Si^{+} + O_2^{+}$ $(faint)$

Interestingly, similar dissociation tracks to those of the albite plot are present in the correlation histogram of olivine (Fig. 9b and Fig. SI4-3c in SI 4), but they are less intense. In the olivine plot, however, the diagonal tracks are more numerous and pronounced. These tracks indicate~~mark~~ the late co-evaporation of ion pairs, which~~that~~ is the simultaneous evaporation of an ion-type *i* and ion-type *j* after a laser pulse (with a delayed time Δt) and are reflected in the mass spectrum as tails following the peaks (Saxey, 2011). The non-stoichiometry of the olivine compositional estimates is likely partially due to the difficult deconvolution of the numerous peak overlapping caused by the late co-evaporation events.

Notably, barite plot does not display any dissociation tracks and, most importantly, intense diagonal tracks deploy from every node (Fig. 9c). The late evaporated ions depicted by the diagonal tracks contribute to the high background and big thermal tails in the barite spectrum (Figs. SI3-3 and SI4-1 in SI 3 and 4, respectively). It is worth noting that the presence of an intense node corresponding to Ba^{2+} (69 Da) on the diagonal of the barite Saxey plot means that the multiplicity of the ion-pair Ba^{2+}-Ba^{2+} is recorded, that is the Ba^{2+} ion is not strongly affected by the ion-pile up effect (Meisenkothen, et al., 2015). To the contrary, S and O (as elements or combined in molecular species) are probably undercounted because of the pile-up phenomenon; the multiple events of the same isotope with the same charge state are probably not detected for the dead-time and dead-zone of the detector.

To assess the importance of the late evaporation and dissociation events on the chemical composition estimate of the minerals, it is useful to compare two different runs that gave different composition estimates. As-pyrite response to the laser PE and PR was the most variable among the studied minerals. The comparison of two As-pyrite correlation histograms of the PE testing, namely the 30 and 50 pJ runs, demonstrates that the late evaporation of ion-pairs described by the vertical and horizontal lines (ion-type *j* evaporation after the evaporation of the paired ion *i* at the laser pulse) and the ion dissociation (curved lines) play a crucial role in the reliable estimate of the mineral composition (Fig. 8c,d). As the As-pyrite composition becomes less stoichiometric from 30 to 50 pJ (Fig. 3), the tracks of the Saxey plot thicken, and a new faint dissociation track appears relative to the Fe_2S^{2+} molecular ion (Fig. 8d). Noteworthy, the qualitative evaluations of the line thickness of Saxey plots are consistent with the measured mineral's stoichiometry.

The above data processing validates the general knowledge about the detrimental consequences of the ion multiple evaporation events during an APT mineral analysis. However, suitable results were obtained in the present study under particular experimental settings for at least twohree of the five studied minerals.

<Figure 8 here>

<Figure 9 here>

Summary

In this study, five minerals belonging to different class/group have been analyzed by APT to test the influence of the laser pulse energy (PE) and rate (PR) on the quality of the output parameters and the compositional estimates. The variation of the background, mass resolution and

multiple event percentage have been considered as indicators for the good outcome of the analysis together with the elemental stoichiometric ratios for each mineral.

The main results obtained may be summarized as follows:

1. The calculated baseline of each analyzed mass spectrum has proved to be a better proxy for the overall background level than the values retrieved from the data set reconstruction (by IVAS software) that may be affected by peak overlapping. The baseline and the mass resolution variation with the PE (10-50 pJ range) and PR (100-250 kHz range) is reasonable for insulator materials: the higher the laser pulse energy, the higher and lower the background level and mass resolution, respectively; the higher the laser pulse rate, the lower and higher the background level and mass resolution, respectively. This applies for all the studied minerals except for the As-pyrite that has the higher thermal conductivity and the lower optical band gap.

2. The multiple events varied in a narrow range for all the studied minerals and experimental conditions. Nevertheless, the data processing performed in the present work suggests that the careful study of the multiple hits, pulse energy, and pulse rate dependence on the CSR and O-IF (proxies for the surface electric field strength) may be a good strategy to evaluate the efficiency of the atom evaporation during an APT analysis.

3. The analysis of the correlation histograms (Saxey plots) of the multiple events and the estimates of the chemical composition of the minerals indicate that the late evaporation of ion pairs and the molecular ion dissociation are the main causes leading to element deficit during an APT run, pointing to a strong detrimental effect of the ion pile-up phenomenon.

4. Special attention must be given to the APT specimen preparation and analysis of minerals with alkali metals in their structural formula (such as alkali feldspar, e.g., albite) since FIB operations may introduce undesired artifacts due to alkali-ion loss.

Acknowledgements

This research was funded by the U.S. National Science Foundation (NSF), grant numbers EAR-1647012 and EAR-2019870. Microscopy work (FIB-SEM) was performed using instruments owned and maintained by the Alabama Analytical Research Center (AARC), supported by The University of Alabama. The authors thank the reviewers for the helpful suggestions and comments provided.

Statements and Declarations

The authors have no competing interests to declare that are relevant to the content of this article.

References

ALDERTON, D. (2021). Olivines. In *Encyclopedia of Geology (Second Edition)*, Alderton, D. and Elias, S. A. (Eds.), pp. 301-309. Oxford: Academic Press.

BACHHAV, M., DANOIX, F., HANNOYER, B., BASSAT, J.M. & DANOIX, R. (2013). Investigation of O-18 enriched hematite (α-Fe2O3) by laser assisted atom probe tomography. International Journal of Mass Spectrometry **335**, 57-60.

BACHHAV, M.N., DANOIX, R., VURPILLOT, F., HANNOYER, B., OGALE, S.B. & DANOIX, F. (2011). Evidence of lateral heat transfer during laser assisted atom probe tomography analysis of large band gap materials. Applied Physics Letters **99**(8), 084101.

BLUM, T.B., DARLING, J.R., KELLY, T.F., LARSON, D.J., MOSER, D.E., PEREZ-HUERTA, A., PROSA, T.J., REDDY, S.M., REINHARD, D.A. & SAXEY, D.W. (2018). Best Practices for Reporting Atom Probe Analysis of Geological Materials. In *Microstructural Geochronology*, Moser, D. E., Corfu, F., Darling, J. R., Reddy, S. M. and Tait, K. T. (Eds.), pp. 369-373. American Geophysical Union

BROWN, J.M., ABRAMSON, E.H. & ANGEL, R.J. (2006). Triclinic elastic constants for low albite. Phys Chem Minerals **33**(4), 256-265.

CAPPELLI, C. & PÉREZ-HUERTA, A. (2020). Effect of crystallographic orientation on atom probe tomography geochemical data? Micron **137**, 102910.

CAPPELLI, C., PÉREZ-HUERTA, A., ALAM, S.B. & PROZOROV, T. (2021a). Atom Probe Tomography Analysis of Mica. Microscopy and Microanalysis, 1-14.

CAPPELLI, C., SMART, S., STOWELL, H. & PÉREZ-HUERTA, A. (2021b). Exploring Biases in Atom Probe Tomography Compositional Analysis of Minerals. Geostandards and Geoanalytical Research **45**(3), 457-476.

CLAUSER, C. & HUENGES, E. (1995). Thermal Conductivity of Rocks and Minerals. In *Rock Physics & Phase Relations*, Ahrens, T. J. (Ed.), pp. 105-126.

CLAVIER, N., PODOR, R. & DACHEUX, N. (2011). Crystal chemistry of the monazite structure. Journal of the European Ceramic Society **31**(6), 941-976.

COCOCCIONI, M. & DE GIRONCOLI, S. (2005). Linear response approach to the calculation of the effective interaction parameters in the LDA+U method. Physical Review B **71**(3), 035105.

CORKHILL, C.L. & VAUGHAN, D.J. (2009). Arsenopyrite oxidation – A review. Applied Geochemistry **24**(12), 2342-2361.

DALY, L., LEE, M.R., DARLING, J.R., MCCARROL, I., YANG, L., CAIRNEY, J., FORMAN, L.V., BLAND, P.A., BENEDIX, G.K., FOUGEROUSE, D., RICKARD, W.D.A., SAXEY, D.W., REDDY, S.M., SMITH, W. & BAGOT, P.A.J. (2021). Developing Atom Probe Tomography of Phyllosilicates in Preparation for Extra-Terrestrial Sample Return. Geostandards and Geoanalytical Research **45**, 427-441.

DEVARAJ, A., COLBY, R., HESS, W.P., PEREA, D.E. & THEVUTHASAN, S. (2013). Role of Photoexcitation and Field Ionization in the Measurement of Accurate Oxide Stoichiometry by Laser-Assisted Atom Probe Tomography. The Journal of Physical Chemistry Letters 4(6), 993-998.

DEVARAJ, A., PEREA, D.E., LIU, J., GORDON, L.M., PROSA, T.J., PARIKH, P., DIERCKS, D.R., MEHER, S., KOLLI, R.P., MENG, Y.S. & THEVUTHASAN, S. (2017). Three-dimensional nanoscale characterisation of materials by atom probe tomography. International Materials Reviews **63**(2), 68-101.

DI RUSSO, E., BLUM, I., HOUARD, J., DA COSTA, G., BLAVETTE, D. & RIGUTTI, L. (2017). Field-Dependent Measurement of GaAs Composition by Atom Probe Tomography. Microscopy and Microanalysis **23**(6), 1067-1075.

DU, A., WAN, C., QU, Z. & PAN, W. (2009). Thermal Conductivity of Monazite-Type $REPO_4$ (RE=La, Ce, Nd, Sm, Eu, Gd). Journal of the American Ceramic Society **92**(11), 2687-2692.

EXERTIER, F., LA FONTAINE, A., CORCORAN, C., PIAZOLO, S., BELOUSOVA, E., PENG, Z., GAULT, B., SAXEY, D.W., FOUGEROUSE, D., REDDY, S.M., PEDRAZZINI, S., BAGOT, P.A.J., MOODY, M.P.,

LANGELIER, B., MOSER, D.E., BOTTON, G.A., VOGEL, F., THOMPSON, G.B., BLANCHARD, P.T., CHIARAMONTI, A.N., REINHARD, D.A., RICE, K.P., SCHREIBER, D.K., KRUSKA, K., WANG, J. & CAIRNEY, J.M. (2018). Atom probe tomography analysis of the reference zircon gj-1: An interlaboratory study. Chemical Geology **495**, 27-35.

FELFER, P.J., GAULT, B., SHA, G., STEPHENSON, L., RINGER, S.P. & CAIRNEY, J.M. (2012). A New Approach to the Determination of Concentration Profiles in Atom Probe Tomography. Microscopy and Microanalysis **18**(2), 359-364.

FOUGEROUSE, D., KIRKLAND, C.L., SAXEY, D.W., SEYDOUX-GUILLAUME, A.-M., ROWLES, M.R., RICKARD, W.D.A. & REDDY, S.M. (2020). Nanoscale Isotopic Dating of Monazite. Geostandards and Geoanalytical Research **44**(4), 637-652.

FOUGEROUSE, D., REDDY, S.M., SAXEY, D.W., ERICKSON, T.M., KIRKLAND, C.L., RICKARD, W.D.A., SEYDOUX-GUILLAUME, A.M., CLARK, C. & BUICK, I.S. (2018). Nanoscale distribution of Pb in monazite revealed by atom probe microscopy. Chemical Geology **479**, 251-258.

FOUGEROUSE, D., REDDY STEVEN, M., SAXEY DAVID, W., RICKARD WILLIAM, D.A., VAN RIESSEN, A. & MICKLETHWAITE, S. (2016). Nanoscale gold clusters in arsenopyrite controlled by growth rate not concentration: Evidence from atom probe microscopy. American Mineralogist, **101**(8),1916-1919.

FOUGEROUSE, D., SAXEY, D.W., RICKARD, W.D.A., REDDY, S.M. & VERBERNE, R. (2021). Standardizing Spatial Reconstruction Parameters for the Atom Probe Analysis of Common Minerals. Microscopy and Microanalysis, 1-10.

GAMAL EL DIEN, H. (2021). Exploring mantle evolution with atom probe tomography. Nature Reviews Earth & Environment **2**(6), 380-380.

GAULT, B., CHIARAMONTI, A., COJOCARU-MIRÉDIN, O., STENDER, P., DUBOSQ, R., FREYSOLDT, C., MAKINENI, S.K., LI, T., MOODY, M. & CAIRNEY, J.M. (2021). Atom probe tomography. Nature Reviews Methods Primers **1**(1), 51.

GAULT, B., LA FONTAINE, A., MOODY, M.P., RINGER, S.P. & MARQUIS, E.A. (2010). Impact of laser pulsing on the reconstruction in an atom probe tomography. Ultramicroscopy **110**(9), 1215-1222.

GAULT, B., MOODY, M.P., CAIRNEY, J.M. & RINGER, S.P. (2012). *Atom probe microscopy*. Springer Science & Business Media.

GAULT, B., SAXEY, D.W., ASHTON, M.W., SINNOTT, S.B., CHIARAMONTI, A.N., MOODY, M.P. & SCHREIBER, D.K. (2016). Behavior of molecules and molecular ions near a field emitter. New Journal of Physics **18**(3), 033031.

GOPON, P., DOUGLAS, J.O., MEISENKOTHEN, F., SINGH, J., LONDON, A.J. & MOODY, M.P. (2021). Atom Probe Tomography for Isotopic Analysis: Development of the $^{34}S/^{32}S$ System in Sulfides. Microscopy and Microanalysis, 1-14.

GORDON, L.M. (2015). Atom Probe Tomography of Feldspars and Aluminosilicate Glasses. Microscopy and Microanalysis **21**(S3), 853-854.

GORDON, L.M., TRAN, L. & JOESTER, D. (2012). Atom Probe Tomography of Apatites and Bone-Type Mineralized Tissues. ACS Nano **6**(12), 10667-10675.

GRIFFITH, E.M. & PAYTAN, A. (2012). Barite in the ocean – occurrence, geochemistry and palaeoceanographic applications. Sedimentology **59**(6), 1817-1835.

HÖVELMANN, J., PUTNIS, A., GEISLER, T., SCHMIDT, B.C. & GOLLA-SCHINDLER, U. (2010). The replacement of plagioclase feldspars by albite: observations from hydrothermal experiments. Contributions to Mineralogy and Petrology **159**(1), 43-59.

JOSEPH, C., FOUGEROUSE, D., SAXEY, D.W., VERBERNE, R., REDDY, S.M. & RICKARD, W.D.A. (2021). Xenotime at the Nanoscale: U-Pb Geochronology and Optimisation of Analyses by Atom Probe Tomography. Geostandards and Geoanalytical Research **45**(3), 443-456.

KARAHKA, M., XIA, Y. & KREUZER, H.J. (2015). The mystery of missing species in atom probe tomography of composite materials. Applied Physics Letters **107**(6), 062105.

KELLY, T.F. & LARSON, D.J. (2012). Atom Probe Tomography 2012. Annual Review of Materials Research **42**(1), 1-31.

KELLY, T.F., VELLA, A., BUNTON, J.H., HOUARD, J., SILAEVA, E.P., BOGDANOWICZ, J. & VANDERVORST, W. (2014). Laser pulsing of field evaporation in atom probe tomography. Current Opinion in Solid State and Materials Science **18**(2), 81-89

KINNO, T., TOMITA, M., OHKUBO, T., TAKENO, S. & HONO, K. (2014). Laser-assisted atom probe tomography of 18O-enriched oxide thin film for quantitative analysis of oxygen. Applied Surface Science **290**, 194-198.

KIRCHHOFER, R., TEAGUE, M.C. & GORMAN, B.P. (2013). Thermal effects on mass and spatial resolution during laser pulse atom probe tomography of cerium oxide. Journal of Nuclear Materials **436**(1), 23-28.

KIRUBANITHY, M., IRUDAYARAJ, A.A., RAJ, A.D. & MANIKANDAN, S. (2015). Synthesis, Characterization and Photoluminescence Behaviours of $CePO_4$ and Tb-doped $CePO_4$ Nanostructures. Materials Today: Proceedings **2**(9, Part A), 4344-4347.

KROT, A.N., KEIL, K., SCOTT, E.R.D., GOODRICH, C.A. & WEISBERG, M.K. (2014). 1.1 - Classification of Meteorites and Their Genetic Relationships. In *Treatise on Geochemistry (Second Edition)*, Holland, H. D. and Turekian, K. K. (Eds.), pp. 1-63. Oxford: Elsevier.

LA FONTAINE, A., PIAZOLO, S., TRIMBY, P., YANG, L. & CAIRNEY, J.M. (2017). Laser-Assisted Atom Probe Tomography of Deformed Minerals: A Zircon Case Study. Microscopy and Microanalysis **23**(2), 404-413.

LA FONTAINE, A., ZAVGORODNIY, A., LIU, H., ZHENG, R., SWAIN, M. & CAIRNEY, J. (2016). Atomic-scale compositional mapping reveals Mg-rich amorphous calcium phosphate in human dental enamel. Science Advances **2**(9), e1601145.

LARSON, D.J., PROSA, T., ULFIG, R.M., GEISER, B.P. & KELLY, T.F.J.N.Y., US: SPRINGER SCIENCE. (2013). *Local electrode atom probe tomography*. New York: US: Springer Science.

LEE, B.E.J., LANGELIER, B. & GRANDFIELD, K. (2021). Visualization of Collagen–Mineral Arrangement Using Atom Probe Tomography. Advanced Biology **5**(9), 2100657.

LI, Y.-Q., HE, Q., CHEN, J.-H. & ZHAO, C.-H. (2015). Electronic and chemical structures of pyrite and arsenopyrite. Mineralogical Magazine **79**(7), 1779-1789.

LU, X., SCHREIBER, D.K., NEEWAY, J.J., RYAN, J.V. & DU, J. (2017). Effects of optical dopants and laser wavelength on atom probe tomography analyses of borosilicate glasses. Journal of the American Ceramic Society **100**(10), 4801-4815.

MEISENKOTHEN, F., STEEL, E.B., PROSA, T.J., HENRY, K.T. & PRAKASH KOLLI, R. (2015). Effects of detector dead-time on quantitative analyses involving boron and multi-hit detection events in atom probe tomography. Ultramicroscopy **159**, 101-111.

MILLER, M.K. & FORBES, R.G. (2014). The Art of Specimen Preparation. In *Atom-Probe Tomography: The Local Electrode Atom Probe*, Miller, M. K. and Forbes, R. G. (Eds.), pp. 189-228. Boston, MA: Springer US.

MÜLLER, M., SMITH, G.D.W., GAULT, B. & GROVENOR, C.R.M. (2012). Compositional nonuniformities in pulsed laser atom probe tomography analysis of compound semiconductors. Journal of Applied Physics **111**(6), 064908.

ONUEGBU, S. & OLUYAMO, S. (2020). Opto-Structural (XRD) Characterization of Locally Synthesized Barium Sulfate ($BaSO_4$) Nanoparticles from an Aqueous Solution of Barium Chloride (BaCl2) and Sulfuric Acid (H2SO4). United International Journal for Research & Technology (UIJRT) **2(2)**, pp.22-25.

PENG, Z., VURPILLOT, F., CHOI, P.P., LI, Y., RAABE, D. & GAULT, B. (2018). On the detection of multiple events in atom probe tomography. Ultramicroscopy **189**, 54-60.

PFEIFFER, B., MAIER, J., ARLT, J. & NOWAK, C. (2017). In Situ Atom Probe Deintercalation of Lithium-Manganese-Oxide. Microscopy and Microanalysis **23**(2), 314-320.

PRASAD, A.K. & JAIN, M. (2018). Breakdown of Kasha's Rule in a Ubiquitous, Naturally Occurring, Wide Bandgap Aluminosilicate (Feldspar). Scientific Reports **8**(1), 810.

PROSA, T.J., STRENNEN, S., OLSON, D., LAWRENCE, D. & LARSON, D.J. (2019). A Study of Parameters Affecting Atom Probe Tomography Specimen Survivability. Microscopy and Microanalysis **25**(2), 425-437.

RAPP, R.P. & WATSON, E.B. (1986). Monazite solubility and dissolution kinetics: implications for the thorium and light rare earth chemistry of felsic magmas. Contributions to Mineralogy and Petrology **94**(3), 304-316.

REDDY, S.M., SAXEY, D.W., RICKARD, W.D.A., FOUGEROUSE, D., MONTALVO, S.D., VERBERNE, R. & VAN RIESSEN, A. (2020). Atom Probe Tomography: Development and Application to the Geosciences. Geostandards and Geoanalytical Research **44**(1), 5-50.

RILEY, J.R., BERNAL, R.A., LI, Q., ESPINOSA, H.D., WANG, G.T. & LAUHON, L.J. (2012). Atom Probe Tomography of a-Axis GaN Nanowires: Analysis of Nonstoichiometric Evaporation Behavior. ACS Nano **6**(5), 3898-3906.

SANTHANAGOPALAN, D., SCHREIBER, D.K., PEREA, D.E., MARTENS, R.L., JANSSEN, Y., KHALIFAH, P. & MENG, Y.S. (2015). Effects of laser energy and wavelength on the analysis of LiFePO4 using laser assisted atom probe tomography. Ultramicroscopy **148**, 57-66.

SAXEY, D.W. (2011). Correlated ion analysis and the interpretation of atom probe mass spectra. Ultramicroscopy **111**(6), 473-479.

SAXEY, D.W., MOSER, D.E., PIAZOLO, S., REDDY, S.M. & VALLEY, J.W. (2018a). Atomic worlds: Current state and future of atom probe tomography in geoscience. Scripta Materialia **148**, 115-121.

SAXEY, D.W., REDDY, S.M., FOUGEROUSE, D. & RICKARD, W.D.A. (2018b). The Optimization of Zircon Analyses by Laser-Assisted Atom Probe Microscopy. In *Microstructural Geochronology*, Moser, D. E., Corf, F., Darling, J. R., Reddy, S. M. and Tait, K. (Eds.), pp. 293-313.

SCHREIBER, D.K., CHIARAMONTI, A.N., GORDON, L.M. & KRUSKA, K. (2014). Applicability of post-ionization theory to laser-assisted field evaporation of magnetite. Applied Physics Letters **105**(24), 244106.

SEYDOUX-GUILLAUME, A.M., FOUGEROUSE, D., LAURENT, A.T., GARDÉS, E., REDDY, S.M. & SAXEY, D.W. (2019). Nanoscale resetting of the Th/Pb system in an isotopically-closed monazite grain: A combined atom probe and transmission electron microscopy study. Geoscience Frontiers **10**(1), 65-76.

SHANKLAND, T.J. (1968). Band Gap of Forsterite. Science **161**(3836), 51-53.

SILAEVA, E.P., KARAHKA, M. & KREUZER, H.J. (2013). Atom Probe Tomography and field evaporation of insulators and semiconductors: Theoretical issues. Current Opinion in Solid State and Materials Science **17**(5), 211-216.

SUZUKI, A., OHTANI, E., FUNAKOSHI, K., TERASAKI, H. & KUBO, T. (2002). Viscosity of albite melt at high pressure and high temperature. Phys Chem Minerals **29**(3), 159-165.

TACCHETTO, T., REDDY, S.M., SAXEY, D.W., FOUGEROUSE, D., RICKARD, W.D.A. & CLARK, C. (2021). Disorientation control on trace element segregation in fluid-affected low-angle boundaries in olivine. Contributions to Mineralogy and Petrology **176**(7), 59.

TAYLOR, S., DEVARAJ, A., SHIN, Y., TAO, J., BUCHKO, G., SHAW, W. & TARASEVICH, B. (2021). 3D Nanoscale Analysis of Protein-Mineral Nanoparticle Interfaces Using Atom Probe Tomography for Understanding Amelogenesis. Microscopy and Microanalysis **27**(S1), 1268-1269.

VALDERRAMA, B., HENDERSON, H.B., YABLINSKY, C.A., GAN, J., ALLEN, T.R. & MANUEL, M.V. (2015). Investigation of material property influenced stoichiometric deviations as evidenced during UV laser-assisted atom probe tomography in fluorite oxides. Nuclear Instruments and Methods in Physics Research Section B: Beam Interactions with Materials and Atoms **359**, 107-114.

VAUGHAN, D.J. (2021). Sulfides☆. In *Encyclopedia of Geology (Second Edition)*, Alderton, D. and Elias, S. A. (Eds.), pp. 395-412. Oxford: Academic Press.

VERBERNE, R., SAXEY, D.W., REDDY, S.M., RICKARD, W.D.A., FOUGEROUSE, D. & CLARK, C. (2019). Analysis of Natural Rutile (TiO2) by Laser-assisted Atom Probe Tomography. Microscopy and Microanalysis **25**(2), 539-546.

VURPILLOT, F., HOUARD, J., VELLA, A. & DECONIHOUT, B. (2009). Thermal response of a field emitter subjected to ultra-fast laser illumination. Journal of Physics D: Applied Physics **42**(12), 125502

VURPILLOT, F. & OBERDORFER, C. (2015). Modeling Atom Probe Tomography: A review. Ultramicroscopy 159, 202-216.

WEBER, J., BARTHEL, J., BRANDT, F., KLINKENBERG, M., BREUER, U., KRUTH, M. & BOSBACH, D. (2016). Nano-structural features of barite crystals observed by electron microscopy and atom probe tomography. Chemical Geology **424**, 51-59.

WHITE, L.F., KIZOVSKI, T.V., TAIT, K.T., LANGELIER, B., GORDON, L.M., HARLOV, D. & NORBERG, N. (2018). Nanoscale chemical characterisation of phase separation, solid state transformation, and recrystallization in feldspar and maskelynite using atom probe tomography. Contributions to Mineralogy and Petrology **173**(10), 87.

XU, Y., SHANKLAND, T.J., LINHARDT, S., RUBIE, D.C., LANGENHORST, F. & KLASINSKI, K. (2004). Thermal diffusivity and conductivity of olivine, wadsleyite and ringwoodite to 20 GPa and 1373 K. Physics of the Earth and Planetary Interiors **143-144**, 321-336.

YAO, L., GAULT, B., CAIRNEY, J.M. & RINGER, S.P. (2010). On the multiplicity of field evaporation events in atom probe: A new dimension to the analysis of mass spectra. Philosophical Magazine Letters **90**(2), 121-129.

YOO, S.-H., KIM, S.-H., WOODS, E., GAULT, B., TODOROVA, M. & NEUGEBAUER, J. (2022). Origins of the hydrogen signal in atom probe tomography: case studies of alkali and noble metals. New Journal of Physics **24**(1), 013008.

ZUÑIGA-PUELLES, E., CARDOSO-GIL, R., BOBNAR, M., VEREMCHUK, I., HEIDE, G. & GUMENIUK, R. (2021). Electrical and thermal transport properties of natural and synthetic $FeAs_xS_{2-x}$ ($x \leq 0.01$). Journal of Physics and Chemistry of Solids **150**, 109809.

Figure & Table legends

Fig. 1 Voltage history and tip reconstruction of a representative tip of barite for a pulse energy testing run (reference R04474). Dots represent S ions. Black squares indicate the sampled counts for each experimental condition

Fig. 2 Variation of, from top to bottom, background, mass resolution and multiple hits with the laser pulse energy (a-c) and laser pulse rate (d-f), from the output data sets of the mineral APT analysis. The abbreviations in (a) and (d) are ab=albite, Asp=arsenopyrite, bar=barite, ol=olivine, mnz=monazite

Fig. 3 Elemental stoichiometric ratios of APT compositional estimates of albite (ab) and olivine (ol) as a function of the laser pulse energy (a,c) and rate (b,d).

Fig. 4 Elemental stoichiometric ratios of APT compositional estimates of monazite (mnz), barite (bar) and As-pyrite (Asp) as a function of the laser pulse energy (a,c,e) and rate (b,d,f). Dark circle in (e) indicates the closest values to mineral stoichiometry

Fig. 5 Variation of the baseline (calculated by OriginPro-2020) with the laser pulse energy (a) and laser pulse rate (b), from the output data sets of the mineral APT analysis. The abbreviations are ab=albite, Asp=arsenopyrite, bar=barite, ol=olivine, mnz=monazite

Fig. 6 Plotting of the multiple event percentage, laser pulse energy and laser pulse rate as a function of the charge state ratio for albite (a,b), olivine (c,d), monazite (e,f) and As-pyrite (~~h~~g,~~i~~h)

Fig. 7 Plotting of the multiple event percentage, laser pulse energy and laser pulse rate as a function of the oxygen ionic ratio (O-IF=$O^{+}/(O^{+}+O^{2+})$) for albite (a,b), olivine (c,d) and monazite (e,f)

Fig. 8 Correlation histograms (Saxey plots) of selected ranges of mass-to-charge state ratio (M/n) of a,b) monazite (250 kHz run of PR testing), c) As-pyrite 30 pJ run and d) As-pyrite 50 pJ run of the PE testing. In b) the image is a different M/n range of the same plot in a). Horizontal, vertical and diagonal lines correspond to late evaporation events. Curve tracks, marked by red lines in b) and c), correspond to dissociation of molecular species. The numbers in c) indicates the estimated dissociation reactions. The black arrow in d) indicates a new dissociation track (see main text for explanation).

Fig. 9 Correlation histograms (Saxey plots) of selected ranges of mass-to-charge state ratio (M/n) of a) albite, b) olivine, and c) barite (all 30 pJ runs of PE testing). Horizontal, vertical and diagonal lines correspond to late evaporation events. Curve tracks correspond to dissociation of molecular species.

Table 1 Thermal conductivity (estimated in the temperature range 25-30°C) and band gap of the studied minerals

Table 2 Summary of the input and output parameter's values of the APT analysis performed in this study and reported in other studies for the same minerals

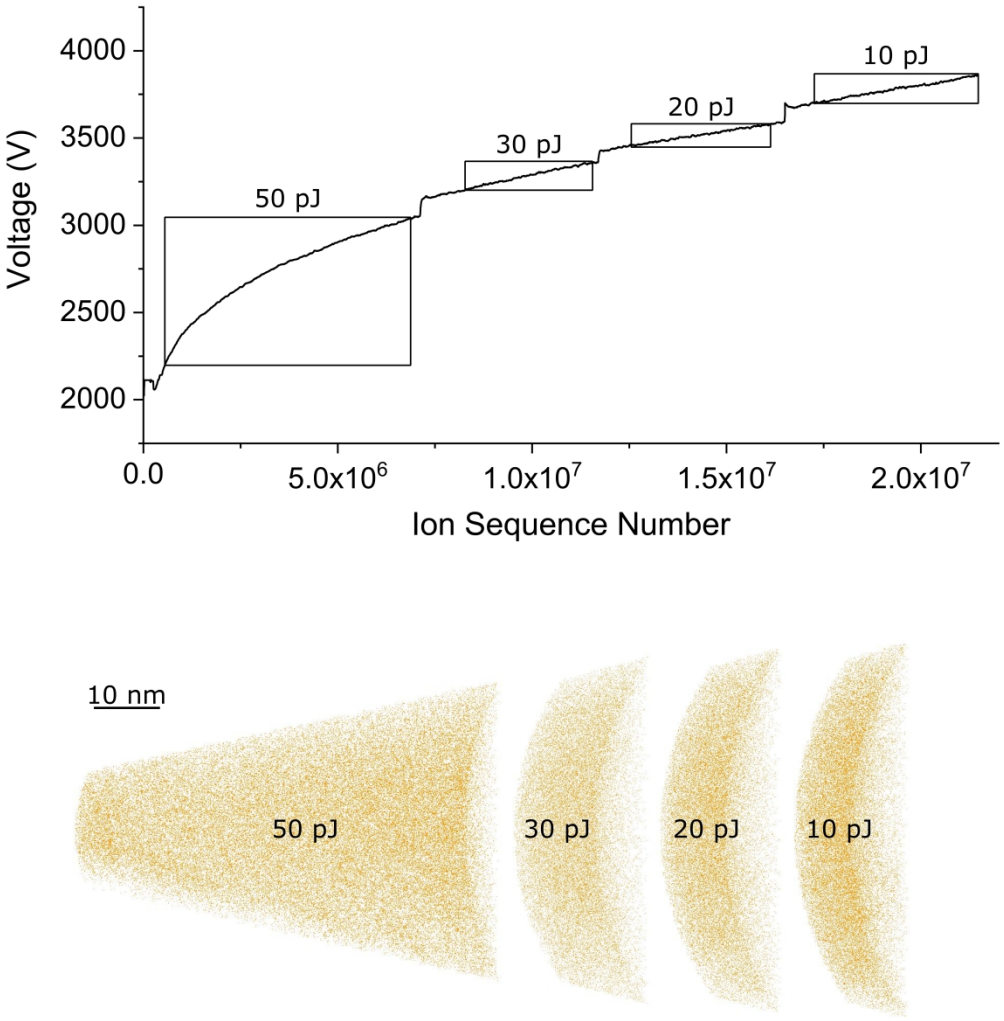

Fig. 1 Voltage history and tip reconstruction of a representative tip of barite for a pulse energy testing run (reference R04474). Dots represent S ions. Black squares indicate the sampled counts for each experimental condition

454x467mm (600 x 600 DPI)

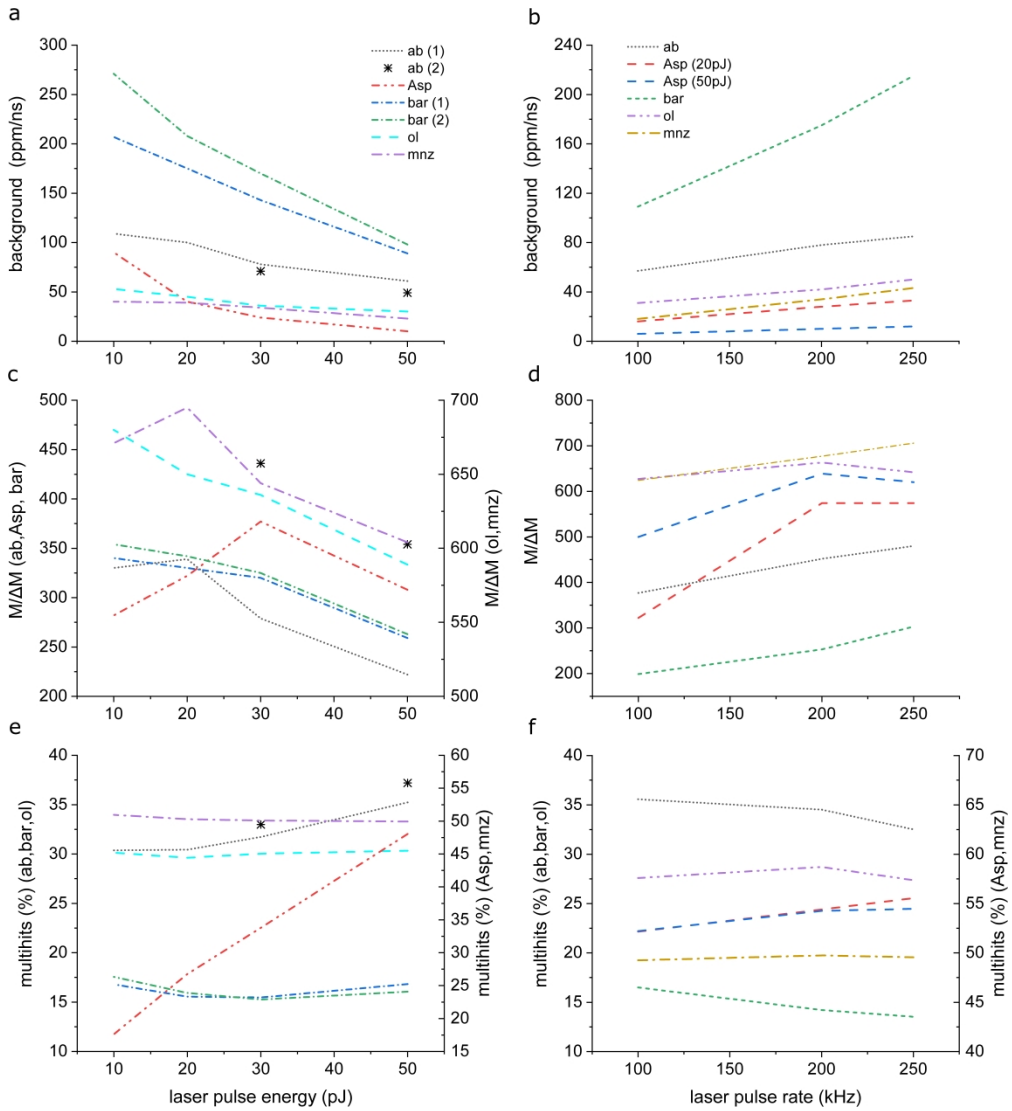

Fig. 2 Variation of, from top to bottom, background, mass resolution and multiple hits with the laser pulse energy (a-c) and laser pulse rate (d-f), from the output data sets of the mineral APT analysis. The abbreviations in (a) and (d) are: ab=albite, Asp=arsenopyrite, bar=barite, ol=olivine, mnz=monazite

505x555mm (600 x 600 DPI)

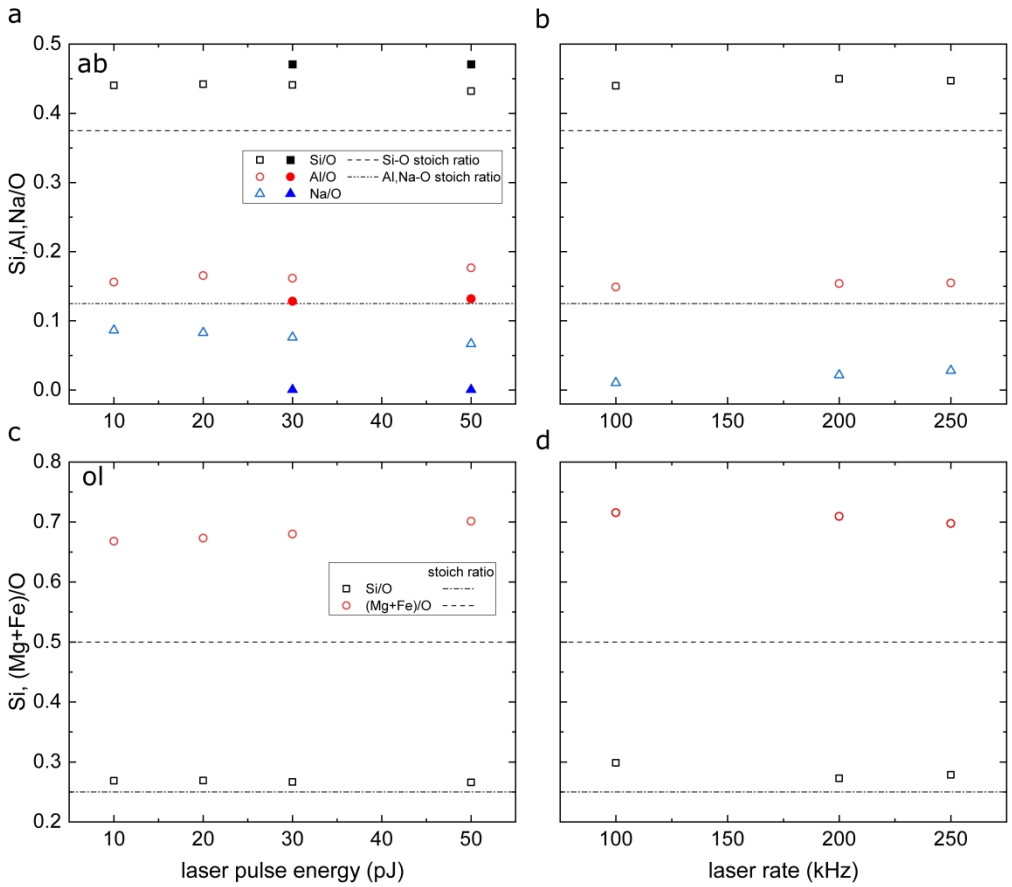

Fig. 3 Elemental stoichiometric ratios of APT compositional estimates of albite (ab) and olivine (ol) as a function of the laser pulse energy (a,c) and rate (b,d)

416x363mm (600 x 600 DPI)

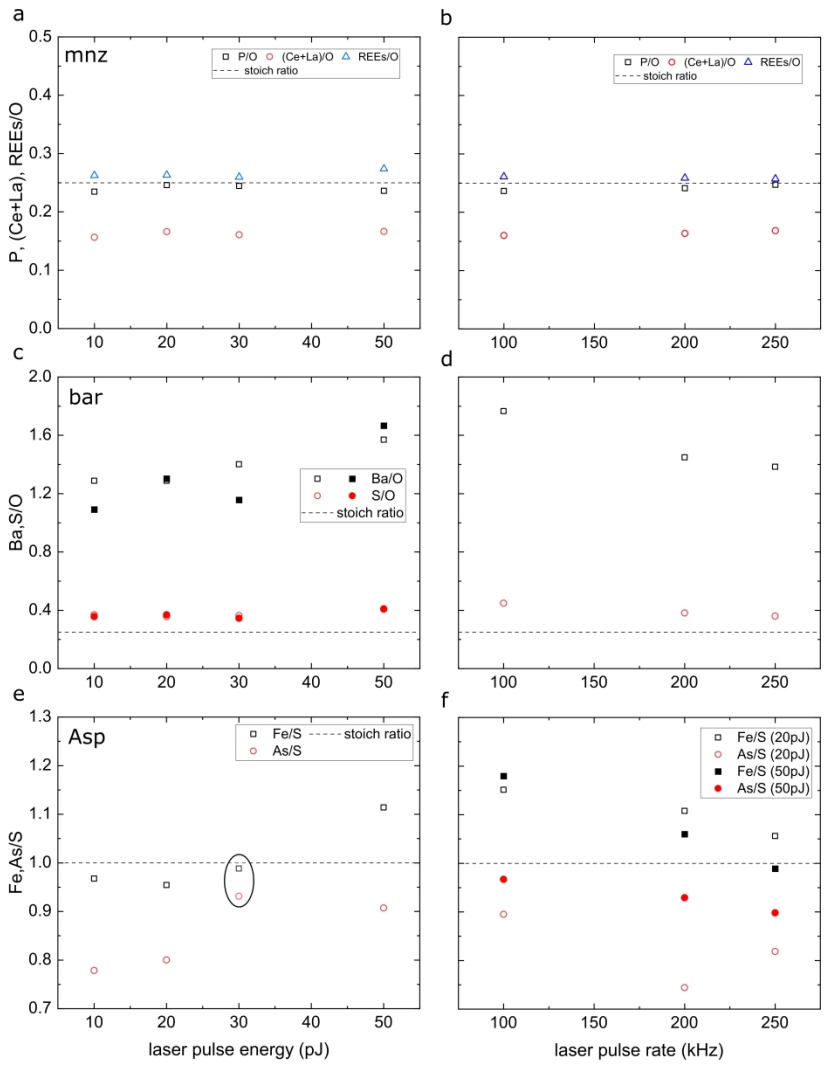

Fig. 4 Elemental stoichiometric ratios of APT compositional estimates of monazite (mnz), barite (bar) and As-pyrite (Asp) as a function of the laser pulse energy (a,c,e) and rate (b,d,f). Dark circle in (e) indicates the closest values to mineral stoichiometry

444x616mm (600 x 600 DPI)

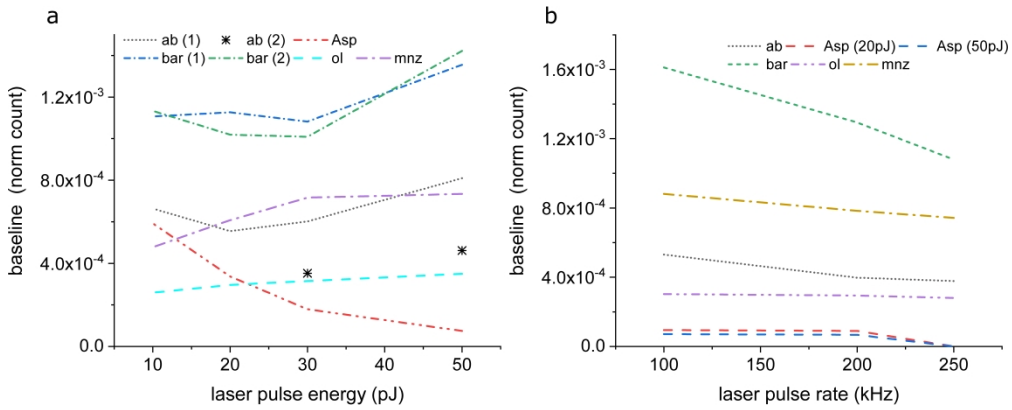

Fig. 5 Variation of the baseline (calculated by OriginPro-2020) with the laser pulse energy (a) and laser pulse rate (b), from the output data sets of the mineral APT analysis. The abbreviations are ab=albite, Asp=arsenopyrite, bar=barite, ol=olivine, mnz=monazite

480x191mm (600 x 600 DPI)

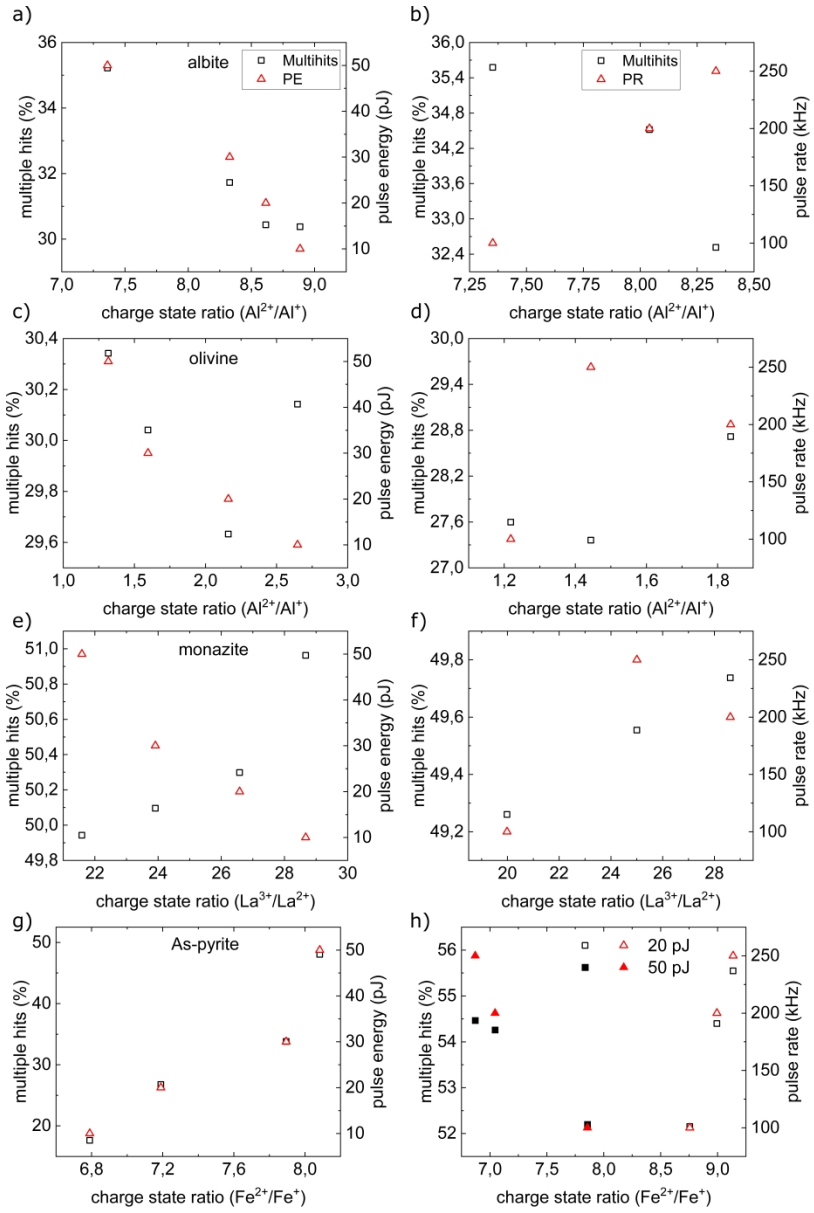

Fig. 6 Plotting of the multiple event percentage, laser pulse energy and laser pulse rate as a function of the charge state ratio for albite (a,b), olivine (c,d), monazite (e,f) and As-pyrite (g,h)

525x783mm (600 x 600 DPI)

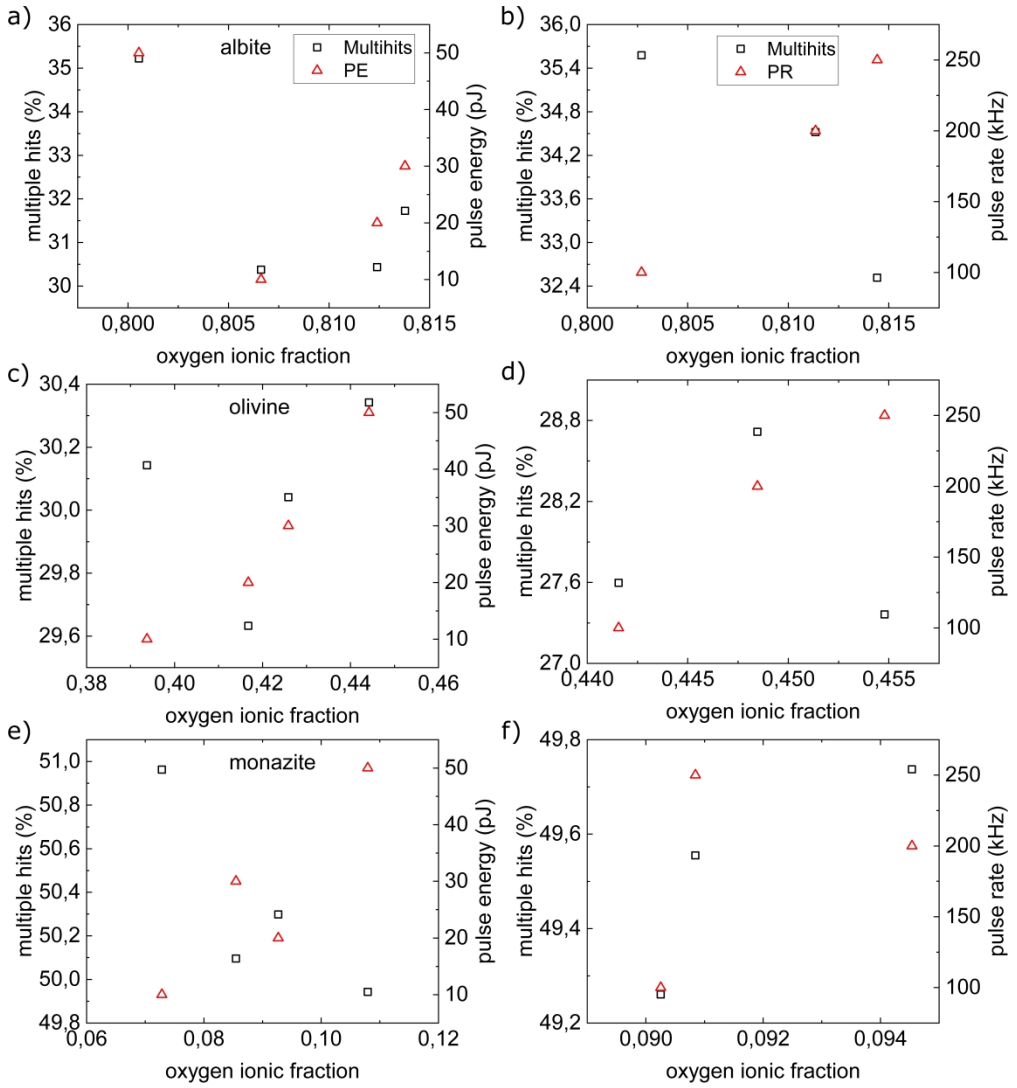

Fig. 7 Plotting of the multiple event percentage, laser pulse energy and laser pulse rate as a function of the oxygen ionic ratio (O-IF=O+/(O++O2+) for albite (a,b), olivine (c,d) and monazite (e,f)

528x568mm (600 x 600 DPI)

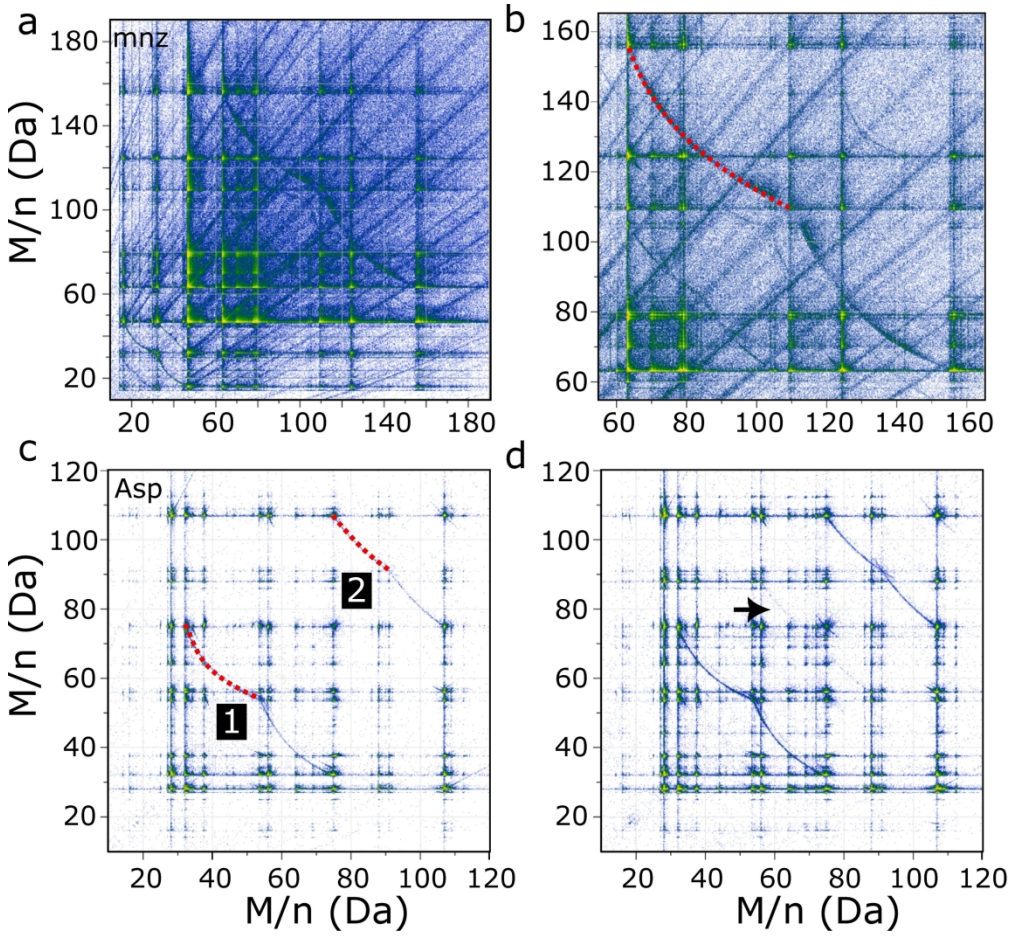

Fig. 8 Correlation histograms (Saxey plots) of selected ranges of mass-to-charge state ratio (M/n) of a,b) monazite (250 kHz run of PR testing), c) As-pyrite 30 pJ run and d) As-pyrite 50 pJ run of the PE testing. In b) the image is a different M/n range of the same plot in a). Horizontal, vertical and diagonal lines correspond to late evaporation events. Curve tracks, marked by red lines in b) and c), correspond to dissociation of molecular species. The numbers in c) indicates the estimated dissociation reactions. The black arrow in d) indicates a new dissociation track (see main text for explanation).

212x197mm (300 x 300 DPI)

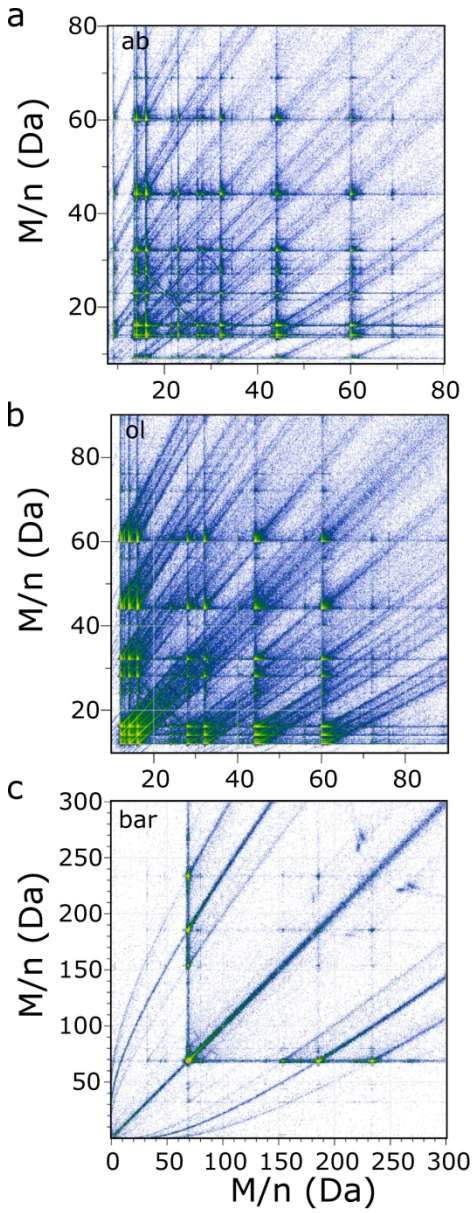

Fig. 9 Correlation histograms (Saxey plots) of selected ranges of mass-to-charge state ratio (M/n) of a) albite, b) olivine, and c) barite (all 30 pJ runs of PE testing). Horizontal, vertical and diagonal lines correspond to late evaporation events. Curve tracks correspond to dissociation of molecular species.

111x287mm (300 x 300 DPI)

	Thermal conductivity	Optical band gap
Mineral	W m-1 K-1	eV
barite*	1.72	4
albite*	2.34	7.7
monazite (LN)**	4	5.28
olivine (Fe)†	4.1	7.5
As-pyrite‡	22.4	0.78

*TC (Clauser and Huenges 1995); BG-barite (Onuegbu and Oluyamo) BG-albite (Prasad and Jain 2018)

**TC approximation from (Du et al 2009); BG (Kirubanithy et al 2015)

†TC approximation from (Clauser and Huenges 1995) and (Xu et al 2004); BG (Shankland 1968)

‡TC (Zuñiga-Puelles et al 2021); BG (Li et al 2015)

Preset	This study - LEAP 5000 XS (T 30 K)		other studies	
	PE testing DR 0.5%, PR 125 kHz	PR testing DR 0.5%, PE 50 pJ		
	albite		LEAP 4000XHR - White et al. 2018	- Gordon (2015)
conditions	10, 20, 30, 50 pJ	100, 200, 250 kHz	T 60.4 K, PR 200 kHz, PE 100 pJ	-
background (ppm/ns)	109, 100, 78, 61	57, 78, 82	-	-
mass resolution (M/ΔM)	330, 339, 279, 222	377, 452, 480	-	-
multi-hits (%)	30.4, 30.4, 31.7, 35.2	35.6, 34.5, 32.5	-	-
stoichiometry	non-stoichiometric	non-stoichiometric	non-stoichiometric	-
	As-pyrite		LEAP 4000X HR - Fougerouse et al. 2021	LEAP 4000X HR - Fougerouse et al. 2016
conditions	10, 20, 30, 50 pJ	100, 200, 250 kHz (20 pJ) 100, 200, 250 kHz (50 pJ)	T 60 K, PR 125 kHz, PE 35 pJ, DR 1%	T 55 K, PR 125 kHz, PE 45-50 pJ, DR 1%
background (ppm/ns)	90, 40, 24, 10	16, 28, 33 6, 10, 12	2	-
mass resolution (M/ΔM)	282, 322, 377, 308	322, 574, 574 500, 639, 620	855-891	-
multi-hits (%)	17.6, 26.8, 33.8, 48.1	52.2, 54.4, 55.5 52.2, 54.3, 54.5	35-37	-
stoichiometry	stoichiometric at 30pJ	non-stoichiometric	-	non-stoichiometric
	barite		LEAP 5000 XS - Cappelli and Pérez-Huerta 2020	LEAP 4000X HR - Weber et al. 2016
conditions	10, 20, 30, 50 pJ (1) 10, 20, 30, 50 pJ (2)	100, 200, 250 kHz	T 30 K, PR 125 kHz, PE 30 pJ, DR 0.5%	T 50 K, PR 160-250 kHz, PE 4-55 pJ, DR 0.5%
background (ppm/ns)	207, 175, 143, 89 271, 208, 170, 98	109, 175, 215	10-33	-
mass resolution (M/ΔM)	340, 330, 320, 259 354, 342, 325, 263	199, 253, 303	327-403	-

multi-hits (%)	16.8, 15.6, 15.5, 16.8 17.6, 15.9, 15.3, 16.0	16.5, 14.2, 13.5	19-20	-
stoichiometry	non-stoichiometric	non-stoichiometric	non-stoichiometric	non-stoichiometric
	monazite		LEAP 4000X HR - Seydoux-Guillaume et al. 2019	LEAP 4000X HR - Fougerouse et al. 2021*
conditions	10, 20, 30, 50 pJ	100, 200, 250 kHz	T 30-50 K, PR 125 kHz, PE 100 pJ, DR 1%	T 60 K, PR 125 kHz, PE 300 pJ, DR 1%
background (ppm/ns)	40, 39, 34, 23	18, 34, 43	20-23	11
mass resolution (M/ΔM)	671, 695, 644, 604	624, 677, 706	1090-1129	1009-1046
multi-hits (%)	51.0, 50.3, 50.1, 50.0	49.3, 49.7, 49.6	32-36	27-28
stoichiometry	stoichiometric	stoichiometric	non-stoichiometric	-
	olivine		LEAP 4000X HR - Fougerouse et al. 2021	LEAP 4000X HR - Tacchetto et al. 2021
conditions	10, 20, 30, 50 pJ	100, 200, 250 kHz	T 60 K, PR 200 kHz, PE 150 pJ, DR 1%	T 50-60 K, PR 200 kHz, PE 80-150 pJ, DR 0.8%
background (ppm/ns)	53, 45, 36, 30	31, 42, 50	18-25	12-25
mass resolution (M/ΔM)	680, 650, 636, 589	627, 663, 642	803-951	1006-1096
multi-hits (%)	30.1, 29.6, 30.0, 30.3	27.6, 28.7, 27.4	23-24	20-26
stoichiometry	non-stoichiometric	non-stoichiometric	-	-

*see also Fougerouse et al. 2020

Supplementary information

Testing the influence of laser pulse energy and rate in the atom probe tomography analysis of minerals

Chiara CAPPELLI[1,*] and Alberto PÉREZ-HUERTA[1]

[1]*Department of Geological Sciences, The University of Alabama, Tuscaloosa, AL 35487, USA*

*Corresponding author – E-mail: ccappelli@ua.edu

Supplementary 1. Running conditions and output data

Table SI1-1. Instrument settings and input and output experimental parameters of albite analysis.

Specimen/Data Set	albite-laser pulse rate-4537				albite-laser pulse energy(1)-4526			albite-laser pulse energy(2)-4538	
Reference	ab-PR100	ab-PR200	ab-PR250	ab-PE50	ab-PE30	ab-PE20	ab-PE10	ab-PE50	ab-PE30
Instrument Model	LEAP 5000 XS				LEAP 5000 XS			LEAP 5000 XS	
Instrument settings								355	355
Laser wavelength (nm)	355	355	355	355	355	355	355	50	30
Laser pulse energy (pJ)	50	50	50	50	30	20	10	125	125
Pulse frequency (kHz)	100	200	250	125	125	125	125		
Evaporation control		Detection rate				Detection rate			Detection rate
Target detection rate (ions/pulse)%	0.5	0.5	0.5	0.5	0.5	0.5	0.5	0.5	0.5
Nominal flight path (mm)	100	100	100	100	100	100	100	100	100
Set point temperature (K)	30	30	30	30	30	30	30	30	30
Chamber pressure (Torr)	4.11E-11	4.11E-11	4.11E-11	4.70E-11	4.70E-11	4.70E-11	4.70E-11	6.40E-11	6.40E-11
Data summary									
Analysis software		IVAS 3.8.10				IVAS 3.8.10			IVAS 3.8.10
Total ions:	2875040	2852388	4990160	2764506	3487788	2897548	2705550	3017098	2887290
Multiple (%)	35.6	34.5	32.5	35.2	31.7	30.4	30.4	37.2	33.0
Reconstructed ions:	2060158	2324296	4193538	2094963	2397577	1848625	1638526	2311430	1953029
Ranged (%)	75.0	73.7	73.6	75.7	74.6	74.1	73.4	76.3	76.4
Mass calib. (peaks/interp.)		Lin. Method				Lin. Method			Lin. Method
(M/ΔM) for $_{16}O^{+}/_{28}Si^{2+}$	377	452	480	222	279	339	330	354	436
$(M/\Delta M_{10})^{c}$	143	174	183	100	125	150	147	133	170
Time independent background (ppm/ns)	57	78	85	61	78	100	109	49	71
Reconstruction									
Final speciment state		Good				Good			Fractured
Pre-/post-analysis imaging		SEM/SEM				SEM/SEM			SEM/SEM
Radius evolution model	Shank	Shank	Shank	Shank	Shank	Shank	Shank	Shank	Shank
Field factor (k)	3.3	3.3	3.3	3.3	3.3	3.3	3.3	3.3	3.3
Image compression factor	1	1.3	1.3	1	1.3	1.3	1.3	1.3	1.3
Assumed E-field (V/nm)	33	33	33	33	33	33	33	33	33
Detector efficiency (%)	80	80	80	80	80	80	80	80	80
Avg. atomic volume (nm^3)	0.02	0.02	0.02	0.02	0.02	0.02	0.02		
$V_{initial}$; V_{final} (V)	5715; 7400	7369;8200	8326;8980	5182;6900	7443;7650	7710;7800	7896;8000	5578;7830	8278;8950
Shank Half Angle (deg)		20.5				21			21
initial tip radius (nm)		22				40			19

Table SI1-2. Instrument settings and input and output experimental parameters of As-pyrite analysis.

Specimen/Data Set	As-pyrite-laser pulse rate (20pJ)-4488			As-pyrite-laser pulse rate (50pJ)-4486			As-pyrite-laser pulse energy-4462			
Reference	Asp-PR100	Asp-PR200	Asp-PR250	Asp-PR100	Asp-PR200	Asp-PR250	Asp-PE50	Asp-PE30	Asp-PE20	Asp-PE10
Instrument Model	LEAP 5000 XS			LEAP 5000 XS			LEAP 5000 XS			
Instrument settings										
Laser wavelength (nm)	355	355	355	355	355	355	355	355	355	355
Laser pulse energy (pJ)	50	50	50	50	50	50	50	30	20	10
Pulse frequency (kHz)	100	200	250	100	200	250	125	125	125	125
Evaporation control	Detection rate			Detection rate			Detection rate			
Target detection rate (ions/pulse)%	0.5	0.5	0.5	0.5	0.5	0.5	0.5	0.5	0.5	0.5
Nominal flight path (mm)	100	100	100	100	100	100	100	100	100	100
Set point temperature (K)	30	30	30	30	30	30	30	30	30	30
Chamber pressure (Torr)	1.20E-10	1.20E-10	1.20E-10	7.50E-11	7.50E-11	7.50E-11	1.60E-10	1.60E-10	1.60E-10	1.60E-10
Data summary										
Analysis software	IVAS 3.8.10			IVAS 3.8.10			IVAS 3.8.10			
Total ions:	4933725	3679100	2189300	4793584	3880954	3423479	5552849	3257258	2902428	3628701
Multiple (%)	52.2	54.4	55.5	52.2	54.3	54.5	48.1	33.8	26.8	17.6
Reconstructed ions:	4458441	3421836	2069006	4656367	3820373	3381835	5330592	2875868	2325620	2346728
Ranged (%)	94.5	92.9	92.3	95.7	96.1	95.9	95.4	93.6	91.0	83.9
Mass calib. (peaks/interp.)	Lin. Method			Lin. Method			Lin. Method			
(M/ΔM) for $_{56}Fe^{2+}$	322	574	574	500	639	620	308	377	322	282
$(M/\Delta M_{10})^c$	109	149	155	132	173	185	118	135	120	87
Time independent background (ppm/ns)	16	28	33	6	10	12	10	24	40	90
Reconstruction										
Final speciment state	Good			Good			Good			
Pre-/post-analysis imaging	SEM/SEM			SEM/SEM			SEM/SEM			
Radius evolution model	Shank	Shank	Shank	Shank	Shank	Shank	Shank	Shank	Shank	Shank
Field factor (k)	3.3	3.3	3.3	4	4	4	4	3.3	3.3	3.3
Image compression factor	1	1.3	1.3	1	1.3	1.3	1	1.3	1.3	1.3
Assumed E-field (V/nm)	33	33	33	33	33	33	33	33	33	33
Detector efficiency (%)	80	80	80	80	80	80	80	80	80	80
Avg. atomic volume (nm^3)	0.0118	0.0118	0.0118	0.0118	0.0118	0.0118	0.0118	0.0118	0.0118	0.0118
$V_{initial}$; V_{final} (V)	2385;4800	5056;5730	5773;6050	20991;4400	4529;5020	5128;5410	2190;4700	5357;5640	6034;6160	6790
Shank Half Angle (deg)	24			19.5			22.5			
initial tip radius (nm)	22			29			25.5			

Table SI1-3. Instrument settings and input and output experimental parameters of barite analysis.

Specimen/Data Set	barite-laser pulse rate-4485			barite-laser pulse energy(1)-4483				barite-laser pulse energy(2)-4474			
Reference	bar-PR100	bar-PR200	bar-PR250	bar-PE50	bar-PE30	bar-PE20	bar-PE10	bar-PE50	bar-PE30	bar-PE20	bar-PE10
Instrument Model	LEAP 5000 XS			LEAP 5000 XS				LEAP 5000 XS			
Instrument settings											
Laser wavelength (nm)	355	355	355	355	355	355	355	355	355	355	355
Laser pulse energy (pJ)	50	50	50	50	30	20	10	50	30	20	10
Pulse frequency (kHz)	100	200	250	125	125	125	125	125	125	125	125
Evaporation control	Detection rate			Detection rate				Detection rate			
Target detection rate (ions/pulse)%	0.5	0.5	0.5	0.5	0.5	0.5	0.5	0.5	0.5	0.5	0.5
Nominal flight path (mm)	100	100	100	100	100	100	100	100	100	100	100
Set point temperature (K)	30	30	30	30	30	30	30	30	30	30	30
Chamber pressure (Torr)	7.20E-11	7.20E-11	7.20E-11	5.60E-11	5.60E-11	5.60E-11	5.60E-11	1.00E-10	1.00E-10	1.00E-10	1.00E-10
Data summary											
Analysis software	IVAS 3.8.10			IVAS 3.8.10				IVAS 3.8.10			
Total ions:	4060783	3546245	3505697	5010804	2692872	2665404	3059244	6079416	3132192	3280662	3764838
Multiple (%)	16.5	14.2	13.5	16.8	15.5	15.6	16.8	16.1	15.3	15.9	17.6
Reconstructed ions:	2689658	2829937	2976865	3740298	1829950	1679735	1748775	4521676	2101502	2048602	2125168
Ranged (%)	54.4	52.5	51.3	51.3	54.5	54.5	53.2	48.8	52.0	51.3	49.8
Mass calib. (peaks/interp.)	Lin. Method			Lin. Method				Lin. Method			
(M/ΔM) for $_{138}Ba^{2+}$	199	253	303	259	320	330	340	263	325	342	354
$(M/\Delta M_{10})^c$	66	125	152	122	149	154	161	114	152	162	157
Time independent background (ppm/ns)	109	175	215	89	143	175	207	98	170	208	271
Reconstruction											
Final speciment state	Good			Good				Good			
Pre-/post-analysis imaging	SEM/SEM			SEM/SEM				SEM/SEM			
Radius evolution model	Shank	Shank	Shank	Shank	Shank	Shank	Shank	Shank	Shank	Shank	Shank
Field factor (k)	3.3	3.3	3.3	3.3	3.3	3.3	3.3	3.3	3.3	3.3	3.3
Image compression factor	1	1.3	1.3	1	1.3	1.3	1.3	1	1.3	1.3	1.3
Assumed E-field (V/nm)	13	13	13	13	13	13	13	13	13	13	13
Detector efficiency (%)	80	80	80	80	80	80	80	80	80	80	80
Avg. atomic volume (nm^3)	0.0634	0.0634	0.0634	0.0634	0.0634	0.0634	0.0634	0.0634	0.0634	0.0634	0.0634
$V_{initial}$; V_{final} (V)	2724;3380	3484;3770	3811;3975	2729;3395	3687;3860	4081;4190	4530;4650	2132;3050	3185;3360	3456;3580	3698;3860
Shank Half Angle (deg)	23.5			25				20			
initial tip radius (nm)	25			20				25.5			

Table SI1-4. Instrument settings and input and output experimental parameters of monazite analysis.

Specimen/Data Set	monazite-laser pulse rate-4556			monazite-laser pulse energy-4555			
Reference	mnz-PR100	mnz-PR200	mnz-PR250	mnz-PE50	mnz-PE30	mnz-PE20	mnz-PE10
Instrument Model	LEAP 5000 XS			LEAP 5000 XS			
Instrument settings							
Laser wavelength (nm)	355	355	355	355	355	355	355
Laser pulse energy (pJ)	50	50	50	50	30	20	10
Pulse frequency (kHz)	100	200	250	125	125	125	125
Evaporation control	Detection rate			Detection rate			
Target detection rate (ions/pulse)%	0.5	0.5	0.5	0.5	0.5	0.5	0.5
Nominal flight path (mm)	100	100	100	100	100	100	100
Set point temperature (K)	30	30	30	30	30	30	30
Chamber pressure (Torr)	7.20E-11	7.20E-11	7.20E-11	5.30E-11	5.30E-11	5.30E-11	5.30E-11
Data summary							
Analysis software	IVAS 3.8.10			IVAS 3.8.10			
Total ions:	3625128	2917928	3095378	4286268	2833812	3206592	3803328
Multiple (%)	49.3	49.7	49.6	49.9	50.1	50.3	51.0
Reconstructed ions:	3282909	2746005	2931835	3909593	2488227	2712771	3137830
Ranged (%)	69.4	70.2	70.2	70.0	72.3	73.2	75.2
Mass calib. (peaks/interp.)	Lin. Method			Lin. Method			
(M/ΔM) for $_{16}O_2^+$	624	677	706	604	644	695	671
$(M/\Delta M_{10})^c$	288	316	313	303	303	321	319
Time independent background (ppm/ns)	18	34	43	23	34	39	40
Reconstruction							
Final speciment state	Good			Good			
Pre-/post-analysis imaging	SEM/SEM			SEM/SEM			
Radius evolution model	Shank	Shank	Shank	Shank	Shank	Shank	Shank
Field factor (k)	4.5	4.5	4.5	4	4	4	4
Image compression factor	1	1.3	1.3	1	1.3	1.3	1.3
Assumed E-field (V/nm)	18	18	18	18	18	18	18
Detector efficiency (%)	80	80	80	80	80	80	80
Avg. atomic volume (nm^3)	0.0118	0.0118	0.0118	0.0118	0.0118	0.0118	0.0118
$V_{initial}$; V_{final} (V)	3742;4900	5081;5480	5568;5880	3705;5030	5212;5560	5663;5940	6059;6270
Shank Half Angle (deg)	24			21			
initial tip radius (nm)	30			43			

Table SI1-5. Instrument settings and input and output experimental parameters of olivine analysis.

Specimen/Data Set	olivine-laser pulse rate-4543			olivine-laser pulse energy-4542			
Reference	ol-PR100	ol-PR200	ol-PR250	ol-PE50	ol-PE30	ol-PE20	ol-PE10
Instrument Model	LEAP 5000 XS			LEAP 5000 XS			
Instrument settings							
Laser wavelength (nm)	355	355	355	355	355	355	355
Laser pulse energy (pJ)	50	50	50	50	30	20	10
Pulse frequency (kHz)	100	200	250	125	125	125	125
Evaporation control	Detection rate			Detection rate			
Target detection rate (ions/pulse)%	0.5	0.5	0.5	0.5	0.5	0.5	0.5
Nominal flight path (mm)	100	100	100	100	100	100	100
Set point temperature (K)	30	30	30	30	30	30	30
Chamber pressure (Torr)	6.90E-11	6.90E-11	6.90E-11	4.90E-11	4.90E-11	4.90E-11	4.90E-11
Data summary							
Analysis software	IVAS 3.8.10			IVAS 3.8.10			
Total ions:	4450080	5692640	5793000	3465180	3281436	3112848	3531888
Multiple (%)	27.6	28.7	27.4	30.3	30.0	29.6	30.1
Reconstructed ions:	3783937	5222547	5400446	3120983	2856840	2596041	2795890
Ranged (%)	74.7	74.6	74.4	73.1	73.4	73.4	75.5
Mass calib. (peaks/interp.)	Lin. Method			Lin. Method			
(M/ΔM) for $_{24}Mg^{2+}$	627	663	642	589	636	650	680
$(M/\Delta M_{10})^{c}$	279	289	296	269	289	290	293
Time independent background (ppm/ns)	31	42	50	29.6	36	45	53
Reconstruction							
Final speciment state	Good			Good			
Pre-/post-analysis imaging	SEM/SEM			SEM/SEM			
Radius evolution model	Shank	Shank	Shank	Shank	Shank	Shank	Shank
Field factor (k)	3.3	3.3	3.3	3.3	3.3	3.3	3.3
Image compression factor	1	1.3	1.3	1	1.3	1.3	1.3
Assumed E-field (V/nm)	21	21	21	21	21	21	21
Detector efficiency (%)	80	80	80	80	80	80	80
Avg. atomic volume (nm^3)	0.0232	0.0232	0.0232	0.0232	0.0232	0.0232	0.0232
$V_{initial}$; V_{final} (V)	4459;5030	5155;5690	6280	4021;4580	4749;5120	5258;5560	6040
Shank Half Angle (deg)	19			21			
initial tip radius (nm)	33.5			32			

Supplementary information

Testing the influence of laser pulse energy and rate in the atom probe tomography analysis of minerals

Chiara CAPPELLI[1,*] and Alberto PÉREZ-HUERTA[1]

[1]*Department of Geological Sciences, The University of Alabama, Tuscaloosa, AL 35487, USA*

*Corresponding author – E-mail: ccappelli@ua.edu

Supplementary 2. APT compositional estimates

albite **NaAlSi3O8**

albite1 (PE)	**10 pJ**	Decomp counts	Atomic fraction	Atomic fraction norm	Atomic error
	K	747	0.0006	0.0006	4.97E-05
	Ca	208	0.0002	0.0002	2.31E-05
	O	723781	0.5935	0.5937	5.20E-04
	Na	62570	0.0513	0.0513	2.83E-04
	Mg	183	0.0002	0.0002	3.28E-05
	Al	112905	0.0926	0.0926	2.94E-04
	Si	318728	0.2614	0.2614	4.21E-04
	Ga	331	0.0003		5.39E-05
	20 pJ				
	K	867	0.0006	0.0006	4.83E-05
	Ca	2	0.0000	0.0000	7.18E-06
	O	828811	0.5907	0.5912	4.79E-04
	Na	68897	0.0491	0.0491	2.59E-04
	Mg	107	0.0001	0.0001	2.67E-05
	Al	137033	0.0977	0.0977	2.73E-04
	Si	366260	0.2610	0.2612	3.95E-04
	Ga	1055	0.0008		6.00E-05
	30 pJ				
	K	880	0.0005	0.0005	4.29E-05
	Ca	240	0.0001	0.0001	1.07E-05
	O	1101926	0.5924	0.5953	4.07E-04
	Na	84113	0.0452	0.0454	2.16E-04
	Mg	179	0.0001	0.0001	2.13E-05
	Al	177925	0.0956	0.0961	2.41E-04
	Si	485696	0.2611	0.2624	3.41E-04
	Ga	9233	0.0050		7.90E-05
	50 pJ				
	K	628	0.0004	0.0004	4.06E-05
	Ca	243	0.0001	0.0001	1.14E-05
	O	970136	0.5830	0.5965	4.37E-04
	Na	64794	0.0389	0.0398	2.12E-04
	Mg	111	0.0001	0.0001	2.09E-05
	Al	171447	0.1030	0.1054	2.60E-04
	Si	419085	0.2518	0.2577	3.60E-04
	Ga	37611	0.0226		1.53E-04

albite2 (PE)		Decomp counts	Atomic fraction	Atomic fraction norm	Atomic error
	30 pJ				
	K	164	1.05E-04	0.0001	3.46E-05
	Ca	111	7.13E-05	0.0001	1.61E-05
	O	969807	0.624362	0.6249	5.05E-04
	Na	608	3.91E-04	0.0004	4.05E-05
	Mg	229	1.47E-04	0.0001	2.73E-05
	Al	124500	0.080153	0.0802	2.36E-04
	Si	456526	0.293911	0.2942	3.66E-04
	Ga	1334	8.59E-04		5.43E-05
	50 pJ				
	K	431	2.29E-04	0.0002	3.80E-05
	Ca	473	2.51E-04	0.0003	1.92E-05
	O	1164660	0.619472	0.6345	4.67E-04
	Na	591	3.14E-04	0.0003	4.24E-05
	Mg	235	1.25E-04	0.0001	2.33E-05
	Al	153407	0.081596	0.0836	2.17E-04
	Si	515887	0.274396	0.2810	3.28E-04
	Ga	44400	0.023616		1.64E-04

albite (PR)	**100 kHz**	Decomp counts	Atomic fraction	Atomic fraction norm	Atomic error
	O	1018074	0.6103	0.6253	4.83E-04
	Na	10780	0.0065	0.0066	8.86E-05
	Mg	175	0.0001	0.0001	2.25E-05
	Al	151477	0.0908	0.0930	2.56E-04
	Si	447717	0.2684	0.2750	3.71E-04
	Ga	39820	0.0239		1.62E-04
	200 kHz				
	O	1158434	0.6120	0.6152	4.47E-04
	Na	25083	0.0133	0.0133	1.16E-04
	Mg	333	0.0002	0.0002	2.87E-05
	Al	178252	0.0942	0.0947	2.44E-04
	Si	520820	0.2751	0.2766	3.51E-04
	Ga	10051	0.0053		8.28E-05
	250 kHz				
	O	2056146	0.6118	0.6134	3.36E-04
	Na	58075	0.0173	0.0173	9.62E-05
	Mg	623	0.0002	0.0002	1.77E-05
	Al	318503	0.0948	0.0950	1.86E-04
	Si	918856	0.2734	0.2741	2.59E-04
	Ga	8420	0.0025		4.85E-05

As-pyrite FeAsS

As-pyrite (PE)	**10 pJ**	Decomp counts	Atomic fraction	Atomic fraction norm	Atomic error	As-pyrite (PR,20pJ)	**100 kHz**	Decomp counts	Atomic fraction	Atomic fraction norm	Atomic error	As-pyrite (PR,50pJ)	**100 kHz**	Decomp counts	Atomic fraction	Atomic fraction norm	Atomic error
	S	324596	0.3642	-	1.22E-03		S	1489670	0.3275	0.3283	2.06E-04		S	1889410	0.3171	0.3179	1.30E-04
	As	252671	0.2835	-	7.35E-03		As	1333150	0.2931	0.2938	1.18E-02		As	1826634	0.3066	0.3073	0.006985
	Fe	314038	0.3523	-	6.77E-04		Fe	1715130	0.3771	0.3780	3.00E-04		Fe	2228203	0.3740	0.3749	2.75E-04
	Ga	0	0.0000		3.49E-06		Ga	10300	0.0023		2.27E-05		Ga	13962	0.0023		3.69E-05
	20 pJ						**200 kHz**						**200 kHz**				
	S	512055	0.3629	0.3631	3.52E-04		S	1268603	0.3504	0.3506	2.55E-04		S	1670947	0.3344	0.3345	1.65E-04
	As	409662	0.2903	0.2905	3.91E-03		As	944093	0.2608	0.2609	1.26E-02		As	1552783	0.3108	0.3109	0.004386
	Fe	488685	0.3464	0.3465	5.40E-04		Fe	1405384	0.3882	0.3884	3.41E-04		Fe	1771219	0.3545	0.3546	3.00E-04
	Ga	525	0.0004		3.22E-05		Ga	2552	0.0007		1.86E-05		Ga	1682	0.0003		2.47E-05
	30 pJ						**250 kHz**						**250 kHz**				
	S	802390	0.3423	0.3425	2.58E-04		S	758885	0.3477	0.3478	3.26E-04		S	1505471	0.3463	0.3464	1.82E-04
	As	747184	0.3187	0.3190	1.05E-02		As	621206	0.2846	0.2847	1.04E-02		As	1351643	0.3109	0.3110	0.002524
	Fe	793010	0.3383	0.3385	4.16E-04		Fe	801571	0.3672	0.3674	4.30E-04		Fe	1488787	0.3424	0.3426	3.21E-04
	Ga	1611	0.0007		2.65E-05		Ga	1056	0.0005		2.10E-05		Ga	1765	0.0004		2.56E-05
	50 pJ																
	S	2230656	0.3301	0.3310	1.20E-04												
	As	2023273	0.2994	0.3003	1.70E-03												
	Fe	2484449	0.3677	0.3687	2.52E-04												
	Ga	18646	0.0028		3.33E-05												

barite	**BaSO4**												
barite1 (PE)		Decomp counts	Atomic fraction	Atomic error	barite2 (PE)		Decomp counts	Atomic fraction	Atomic error	barite (PR)		Decomp counts	Atomic fraction	Atomic error
	10pJ					**10pJ**					**100kHz**			
	S	160428	0.1341	2.81E-04		S	200961	0.1392	2.70E-04		S	179510	0.1368	2.85E-04
	Sr	822	0.0007	7.61E-05		Sr	2232	0.0015	6.35E-05		Sr	1617	0.0012	6.56E-05
	O	434697	0.3634	2.64E-05		O	563601	0.3903	3.37E-05		O	400070	0.3050	3.07E-05
	Ba	559706	0.4679	6.64E-04		Ba	615242	0.4261	6.36E-04		Ba	706258	0.5384	5.97E-04
	La	3286	0.0027	2.44E-04		La	267	0.0002	2.46E-20		La	4722	0.0036	2.24E-04
	Ce	36724	0.0307	3.99E-04		Ce	59695	0.0413	4.32E-04		Ce	18228	0.0139	3.30E-04
	Ni	493	0.0004	8.72E-05		Ni	1951	0.0014	8.63E-05		Ni	1356	0.0010	6.53E-05
	20pJ					**20pJ**					**200kHz**			
	S	162634	0.1309	2.46E-04		S	173319	0.1308	2.54E-04		S	220716	0.1333	2.21E-04
	Sr	1200	0.0010	6.83E-05		Sr	2601	0.0020	6.65E-05		Sr	2638	0.0016	5.55E-05
	O	455823	0.3669	3.13E-05		O	469696	0.3543	1.40E-05		O	578491	0.3493	2.43E-05
	Ba	586900	0.4724	6.50E-04		Ba	611868	0.4616	6.37E-04		Ba	837857	0.5060	5.71E-04
	La	4983	0.0040	2.27E-04		La	3841	0.0029	2.37E-04		La	4931	0.0030	1.93E-04
	Ce	29962	0.0241	3.68E-04		Ce	61798	0.0466	4.24E-04		Ce	9160	0.0055	2.76E-04
	Ni	833	0.0007	7.23E-05		Ni	2432	0.0018	8.01E-05		Ni	2142	0.0013	6.41E-05
	30pJ					**30pJ**					**250kHz**			
	S	159025	0.1287	2.51E-04		S	202209	0.1337	2.39E-04		S	245787	0.1289	1.92E-04
	Sr	1858	0.0015	6.44E-05		Sr	1506	0.0010	6.05E-05		Sr	1559	0.0008	5.28E-05
	O	437893	0.3543	2.67E-05		O	584999	0.3869	2.90E-05		O	683068	0.3582	1.56E-05
	Ba	613715	0.4965	6.61E-04		Ba	676840	0.4476	6.15E-04		Ba	945758	0.4960	5.34E-04
	La	448	0.0004	6.56E-20		La	241	0.0002	4.46E-20		La	7001	0.0037	1.76E-04
	Ce	21877	0.0177	3.68E-04		Ce	45130	0.0298	3.89E-04		Ce	22819	0.0120	2.51E-04
	Ni	1268	0.0010	6.86E-05		Ni	1101	0.0007	6.84E-05		Ni	877	0.0005	6.51E-05
	50pJ					**50pJ**								
	S	277297	0.1349	2.16E-04		S	315145	0.1291	1.80E-04					
	Sr	2201	0.0011	4.98E-05		Sr	2874	0.0012	4.40E-05					
	O	683096	0.3322	5.12E-04		O	770114	0.3155	2.07E-05					
	Ba	1072662	0.5217	2.27E-05		Ba	1282845	0.5255	4.55E-04					
	La	839	0.0004	1.70E-04		La	5524	0.0023	4.63E-05					
	Ce	18366	0.0089	2.34E-04		Ce	62308	0.0255	2.67E-04					
	Ni	1750	0.0009	5.32E-05		Ni	2157	0.0009	4.76E-05					

olivine **$(Mg,Fe)_2SiO_4$**

olivine (PE)

10pJ	Decomp counts	Atomic fraction	Atomic error
Ti	5146	0.0023	1.79E-05
O	1150921	0.5131	2.70E-04
Zr	217	0.0001	1.77E-05
Cr	22	9.72E-06	8.60E-06
Mn	979	0.0004	2.29E-05
Fe	45663	0.0204	7.10E-04
Co	274	0.0001	2.14E-05
Ni	1612	0.0007	2.48E-05
Mg	722918	0.3223	3.78E-04
Al	6285	0.0028	7.83E-05
Si	309187	0.1378	7.24E-04
20pJ			
Ti	7220	0.0036	1.03E-05
O	1016825	0.5112	3.00E-04
Zr	352	0.0002	2.77E-05
Cr	135	0.0001	1.93E-05
Mn	896	0.0005	2.58E-05
Fe	43795	0.0220	7.51E-04
Co	115	0.0001	2.36E-05
Ni	1291	0.0006	2.67E-05
Mg	640364	0.3219	4.03E-04
Al	4710	0.0024	8.43E-05
Si	273393	0.1374	7.70E-04
30pJ			
Ti	3019	0.0014	2.49E-05
O	1119450	0.5115	2.90E-04
Zr	199	0.0001	1.97E-05
Cr	200	0.0001	1.78E-05
Mn	1043	0.0005	2.48E-05
Fe	48838	0.0223	7.19E-04
Co	6	2.73E-06	1.44E-05
Mg	712076	0.3253	3.84E-04
Ni	1433	0.0007	2.75E-05
Al	4288	0.0020	7.98E-05
Si	298221	0.1363	7.36E-04

olivine (PR)

100kHz	Decomp counts	Atomic fraction	Atomic error
Ti	7930.584112	0.00266305	1.91E-05
O	1468833.189	0.49322703	2.45E-04
Zr	520.9026728	1.75E-04	2.48E-05
Cr	317.6218524	1.07E-04	1.55E-05
Mn	1308.973083	4.40E-04	2.06E-05
Fe	47739.77262	0.01603078	6.98E-04
Co	150.4544678	5.05E-05	1.82E-05
Ni	2160.127893	7.25E-04	2.52E-05
Mg	1003216.071	0.33687507	3.31E-04
Al	7562.23458	0.00253936	7.03E-05
Si	438266.3248	0.1471677	7.20E-04
200kHz			
Ti	9574.913257	0.00226266	1.26E-05
O	2123829.579	0.50188435	2.09E-04
Zr	599.4783828	1.42E-04	1.76E-05
Cr	594.7325458	1.41E-04	1.45E-05
Mn	1708.259363	4.04E-04	1.71E-05
Fe	106981.0078	0.02528079	5.37E-04
Co	0	0	7.46E-06
Mg	1399428.841	0.33070046	2.76E-04
Ni	2980.654764	7.04E-04	2.11E-05
Al	6722.457302	0.00158859	5.52E-05
Si	579291.2232	0.1368929	5.52E-04
250kHz			
Ti	11557.37801	0.00266249	1.61E-05
O	2184062.838	0.50314552	2.09E-04
Zr	712.8667915	1.64E-04	1.67E-05
Cr	439.4201856	1.01E-04	1.20E-05
Mn	1796.294804	4.14E-04	1.69E-05
Fe	98892.12214	0.02278191	5.32E-04
Co	430.3701229	9.91E-05	1.55E-05
Mg	1424330.331	0.32812491	2.71E-04
Ni	3136.907653	7.23E-04	2.07E-05
Al	7023.216574	0.00161795	5.43E-05
Si	608435.6976	0.14016616	5.47E-04

To continue

50pJ	Decomp counts	Atomic fraction	Atomic error
Ti	3814	0.0016	2.23E-05

O	1196014	0.5061	2.85E-04
Zr	163	0.0001	1.72E-05
Cr	54	2.28E-05	1.42E-05
Mn	1130	0.0005	2.47E-05
Fe	60482	0.0256	6.79E-04
Co	204	0.0001	2.20E-05
Mg	778113	0.3293	3.71E-04
Ni	1557	0.0007	2.72E-05
Al	3572	0.0015	7.69E-05
Si	318128	0.1346	6.95E-04

monazite **$(Ce,La)PO_4$**

monazite (PE)	Decomp counts	Atomic fraction	Atomic fraction norm	Atomic error	monazite (PR)	Decomp counts	Atomic fraction	Atomic fraction norm	Atomic error
10pJ					**100kHz**				
Gd	66152	0.0183	0.0183	2.31E-04	Gd	74074	0.0211	0.0212	4.35E-04
Tb	4413	0.0012	0.0012	5.60E-05	Tb	4455	0.0013	0.0013	5.05E-05
Dy	16723	0.0046	0.0046	1.15E-04	Dy	17119	0.0049	0.0049	1.09E-04
Ho	693	0.0002	0.0002	2.96E-05	Ho	496	0.0001	0.0001	2.74E-05
Er	2665	0.0007	0.0007	5.14E-05	Er	1182	0.0003	0.0003	5.36E-05
Sr	1530	0.0004	0.0004	3.10E-05	Sr	1743	0.0005	0.0005	3.52E-05
Y	25184	0.0070	0.0070	7.98E-05	Y	22764	0.0065	0.0065	8.56E-05
Zr	9804	0.0027	0.0027	9.84E-05	Zr	5940	0.0017	0.0017	8.15E-05
O	2295709	0.6364	0.6365	1.02E-04	O	2221865	0.6331	0.6373	1.10E-04
Si	15029	0.0042	0.0042	6.63E-05	Si	13804	0.0039	0.0040	6.63E-05
P	538741	0.1494	0.1494	4.34E-05	P	524972	0.1496	0.1506	3.46E-05
Pb	1520	0.0004	0.0004	5.01E-05	Pb	862	0.0002	0.0002	4.90E-05
Ca	39586	0.0110	0.0110	1.21E-04	Ca	39316	0.0112	0.0113	1.24E-04
La	107849	0.0299	0.0299	1.41E-04	La	108700	0.0310	0.0312	1.48E-04
Ce	251093	0.0696	0.0696	2.67E-04	Th	43235	0.0123	0.0124	6.21E-06
Th	38794	0.0108	0.0108	1.70E-06	Ce	247375	0.0705	0.0710	2.71E-04
Pr	12073	0.0033	0.0033	7.07E-05	Pr	8230	0.0023	0.0024	5.14E-05
U	1460	0.0004	0.0004	1.43E-05	U	856	0.0002	0.0002	2.97E-17
Nd	129996	0.0360	0.0360	2.67E-04	Nd	109634	0.0312	0.0314	2.45E-04
Sm	47602	0.0132	0.0132	1.79E-04	Sm	39777	0.0113	0.0114	1.77E-04
Ga	532	0.0001		4.62E-05	Ga	23159	0.0066		1.21E-04
20pJ					**200kHz**				
Gd	58512	0.0178	0.0178	4.51E-04	Gd	57743	0.0188	0.0188	3.73E-04
Tb	5579	0.0017	0.0017	8.08E-05	Tb	2567	0.0008	0.0008	7.30E-05
Dy	12610	0.0038	0.0038	1.16E-04	Dy	13862	0.0045	0.0045	1.13E-04
Ho	112	0.0000	0.0000	3.18E-05	Ho	338	0.0001	0.0001	2.81E-05
Er	1105	0.0003	0.0003	5.22E-05	Er	1433	0.0005	0.0005	5.54E-05
Sr	1646	0.0005	0.0005	3.68E-05	Sr	1162	0.0004	0.0004	3.18E-05
Y	22052	0.0067	0.0067	8.68E-05	Y	19542	0.0064	0.0064	9.33E-05
O	2081503	0.6333	0.6335	1.15E-04	Zr	4850	0.0016	0.0016	8.64E-05
Zr	5681	0.0017	0.0017	9.28E-05	O	1957416	0.6373	0.6377	1.19E-04
Si	10767	0.0033	0.0033	6.31E-05	Si	9757	0.0032	0.0032	6.54E-05
P	512058	0.1558	0.1558	3.93E-05	P	472159	0.1537	0.1538	4.04E-05
Pb	2119	0.0006	0.0006	5.24E-05	Pb	1892	0.0006	0.0006	5.76E-05
Ca	35232	0.0107	0.0107	1.26E-04	Ca	32693	0.0106	0.0107	1.33E-04
La	103895	0.0316	0.0316	1.53E-04	La	94844	0.0309	0.0309	1.59E-04
Ce	241805	0.0736	0.0736	2.90E-04	Ce	225378	0.0734	0.0734	2.98E-04
Th	36857	0.0112	0.0112	1.45E-05	Th	38084	0.0124	0.0124	1.33E-05
Pr	9537	0.0029	0.0029	5.91E-05	Pr	6567	0.0021	0.0021	6.09E-05
Nd	100833	0.0307	0.0307	2.61E-04	U	949	0.0003	0.0003	1.72E-05
U	1283	0.0004	0.0004	1.20E-06	Nd	91969	0.0299	0.0300	2.77E-04
Sm	42649	0.0130	0.0130	1.98E-04	Sm	36226	0.0118	0.0118	1.99E-04
Ga	695	0.0002		5.00E-05	Ga	1918	0.0006		5.79E-05

To continue

	Decomp counts	Atomic fraction	Atomic fraction norm	Atomic error
30pJ				
Gd	61951	0.0220	0.0220	5.11E-04
Tb	4373	0.0016	0.0016	9.21E-05
Dy	12529	0.0044	0.0045	1.26E-04
Ho	333	0.0001	0.0001	3.31E-05
Er	1844	0.0007	0.0007	6.23E-05
Sr	1334	0.0005	0.0005	3.93E-05
Y	18936	0.0067	0.0067	9.26E-05
Zr	5731	0.0020	0.0020	9.28E-05
O	1776917	0.6309	0.6312	1.21E-04
Si	10132	0.0036	0.0036	6.31E-05
P	434315	0.1542	0.1543	4.41E-05
Pb	1904	0.0007	0.0007	5.97E-05
Ca	31108	0.0110	0.0111	1.38E-04
La	84286	0.0299	0.0299	1.63E-04
Ce	208087	0.0739	0.0739	3.13E-04
Th	29151	0.0104	0.0104	6.98E-06
Pr	11140	0.0040	0.0040	8.04E-05
Nd	84632	0.0301	0.0301	3.02E-04
U	830	0.0003	0.0003	1.71E-05
Sm	35448	0.0126	0.0126	2.13E-04
Ga	1315	0.0005		6.04E-05
50pJ				
Gd	86227	0.0211	0.0213	4.13E-04
Tb	6430	0.0016	0.0016	7.76E-05
Dy	14818	0.0036	0.0037	9.76E-05
Ho	314	0.0001	0.0001	2.90E-05
Er	1452	0.0004	0.0004	5.32E-05
Sr	2406	0.0006	0.0006	3.52E-05
Y	27398	0.0067	0.0068	7.94E-05
O	2556013	0.6255	0.6325	1.09E-04
Zr	9315	0.0023	0.0023	8.34E-05
Si	13925	0.0034	0.0034	5.29E-05
P	602851	0.1475	0.1492	3.27E-05
Pb	920	0.0002	0.0002	5.63E-05
Ca	44694	0.0109	0.0111	1.11E-04
La	129724	0.0317	0.0321	1.39E-04
Ce	295868	0.0724	0.0732	2.61E-04
Th	49072	0.0120	0.0121	0
Pr	9261	0.0023	0.0023	5.56E-05
Nd	132812	0.0325	0.0329	2.25E-04
U	2252	0.0006	0.0006	1.63E-05
Sm	55417	0.0136	0.0137	1.76E-04
Ga	45453	0.0111		1.21E-04

	Decomp counts	Atomic fraction	Atomic fraction norm	Atomic error
250kHz				
Gd	62465	0.0191	0.0191	3.46E-04
Tb	2930	0.0009	0.0009	5.37E-05
Dy	13901	0.0042	0.0042	1.13E-04
Ho	491	0.0001	0.0001	2.70E-05
Er	988	0.0003	0.0003	4.79E-05
Sr	1423	0.0004	0.0004	3.34E-05
Y	20603	0.0063	0.0063	9.10E-05
O	2082328	0.6353	0.6354	1.16E-04
Zr	5224	0.0016	0.0016	8.33E-05
Si	12171	0.0037	0.0037	6.57E-05
P	514446	0.1569	0.1570	3.94E-05
Pb	2673	0.0008	0.0008	5.25E-05
Ca	35954	0.0110	0.0110	1.27E-04
La	103475	0.0316	0.0316	1.56E-04
Th	40592	0.0124	0.0124	4.91E-06
Ce	247034	0.0754	0.0754	2.88E-04
Pr	6749	0.0021	0.0021	5.77E-05
Nd	83470	0.0255	0.0255	2.70E-04
U	1026	0.0003	0.0003	1.63E-05
Sm	39227	0.0120	0.0120	1.99E-04
Ga	727	0.0002		3.85E-05

Supplementary information

Testing the influence of laser pulse energy and rate in the atom probe tomography analysis of minerals

Chiara CAPPELLI[1,*] and Alberto PÉREZ-HUERTA[1]

[1]*Department of Geological Sciences, The University of Alabama, Tuscaloosa, AL 35487, USA*

*Corresponding author – E-mail: ccappelli@ua.edu

Supplementary 3. APT spectra

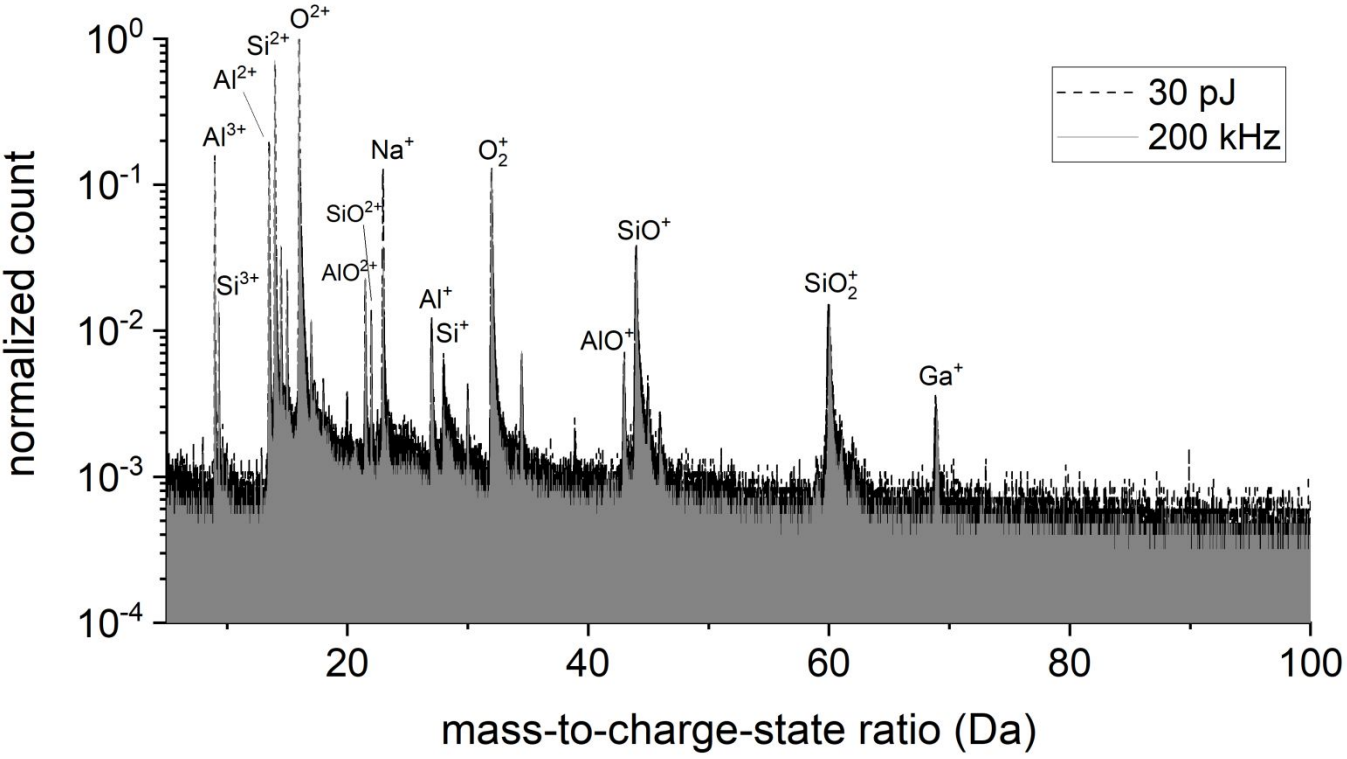

Figure SI3-1. Representative APT spectra of albite (normalization to the highest peak).

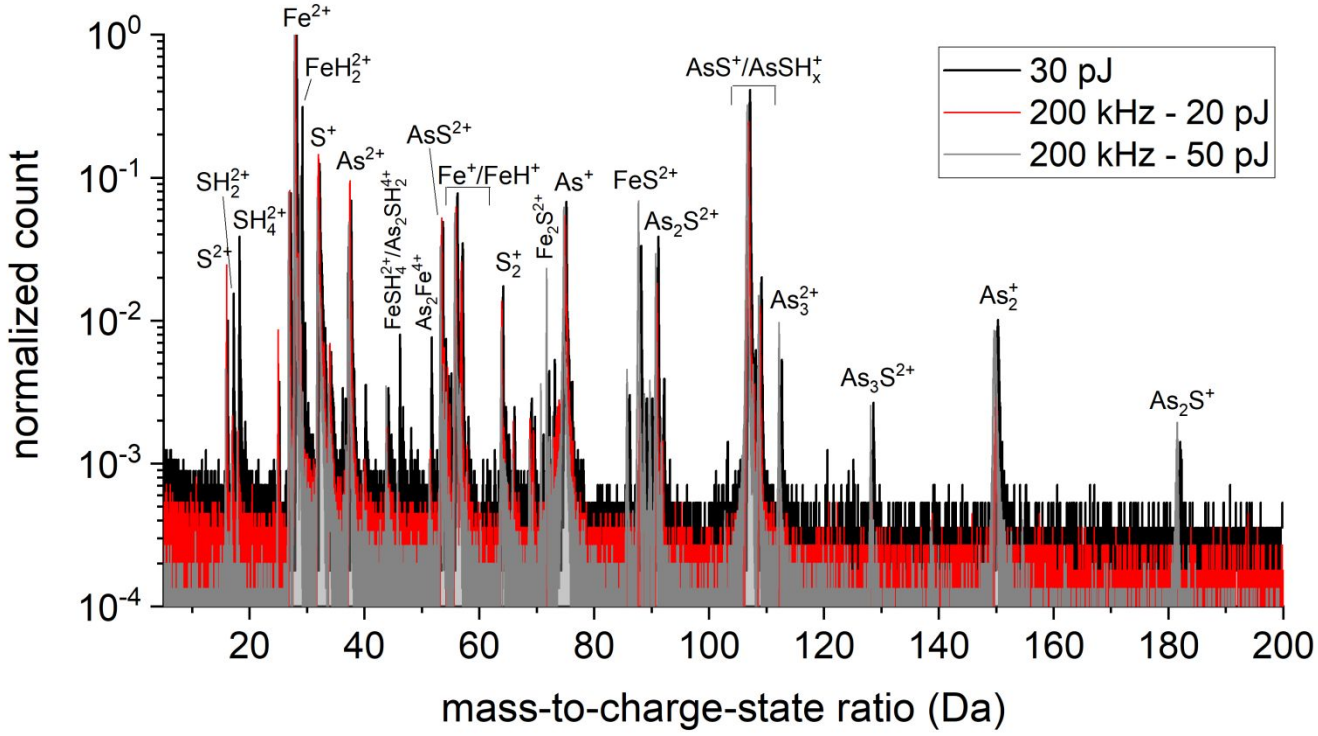

Figure SI3-2. Representative APT spectra of As-pyrite (normalization to the highest peak). Note that a shift of 0.2 and -0.2 Da of the x-axis has been applied to the 30 pJ and 200 kHz - 50 pJ spectra respectively for a better comparison of the peaks.

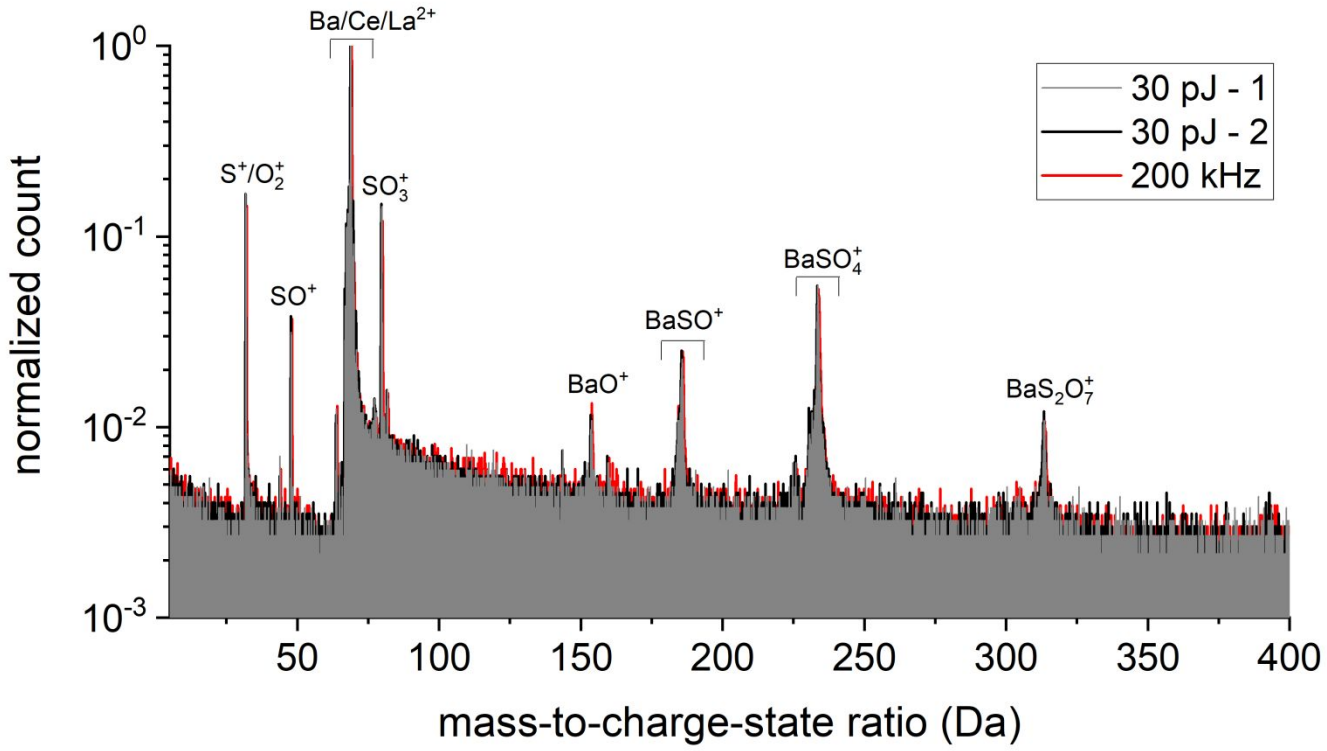

Figure SI3-3. Representative APT spectra of barite (normalization to the highest peak). Note that a shift of 0.2 and -0.2 Da of the x-axis has been applied to the 30 pJ - 2 and 200 kHz spectra respectively for a better comparison of the peaks.

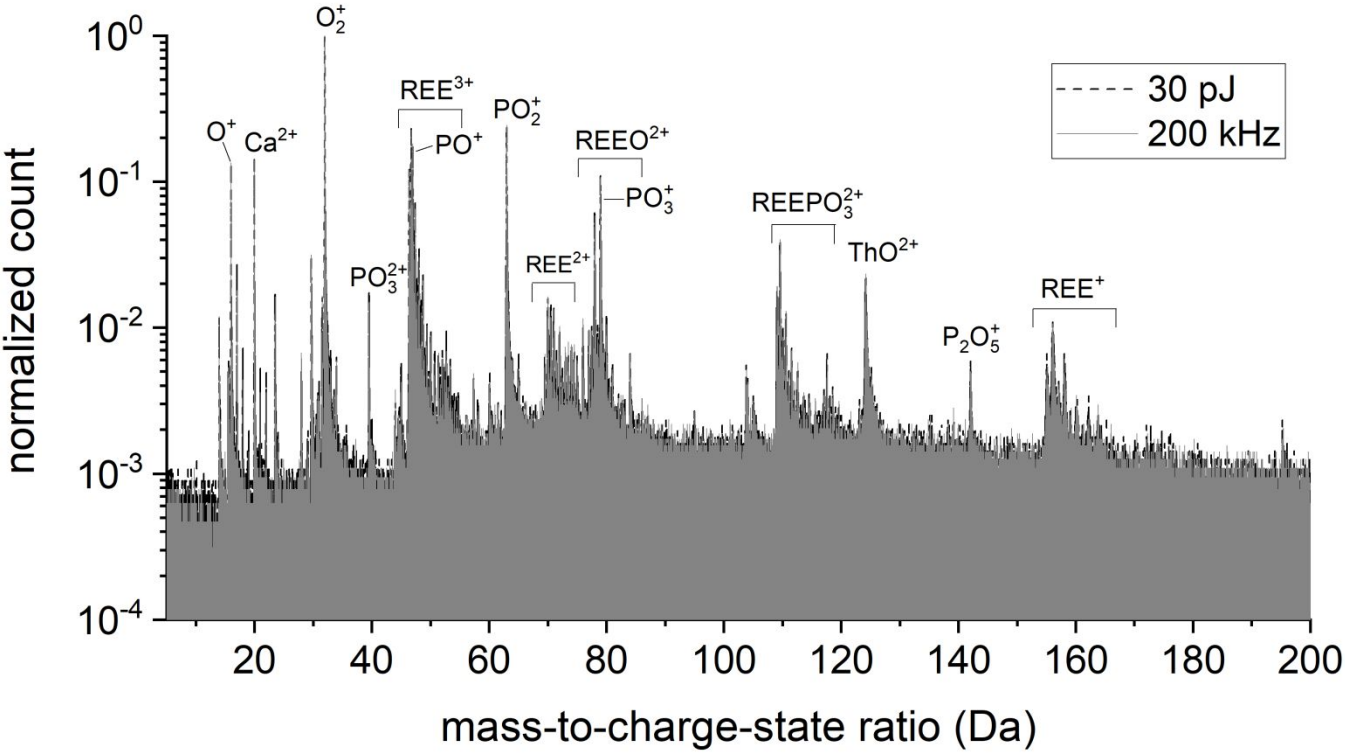

Figure SI3-4. Representative APT spectra of monazite (normalization to the highest peak).

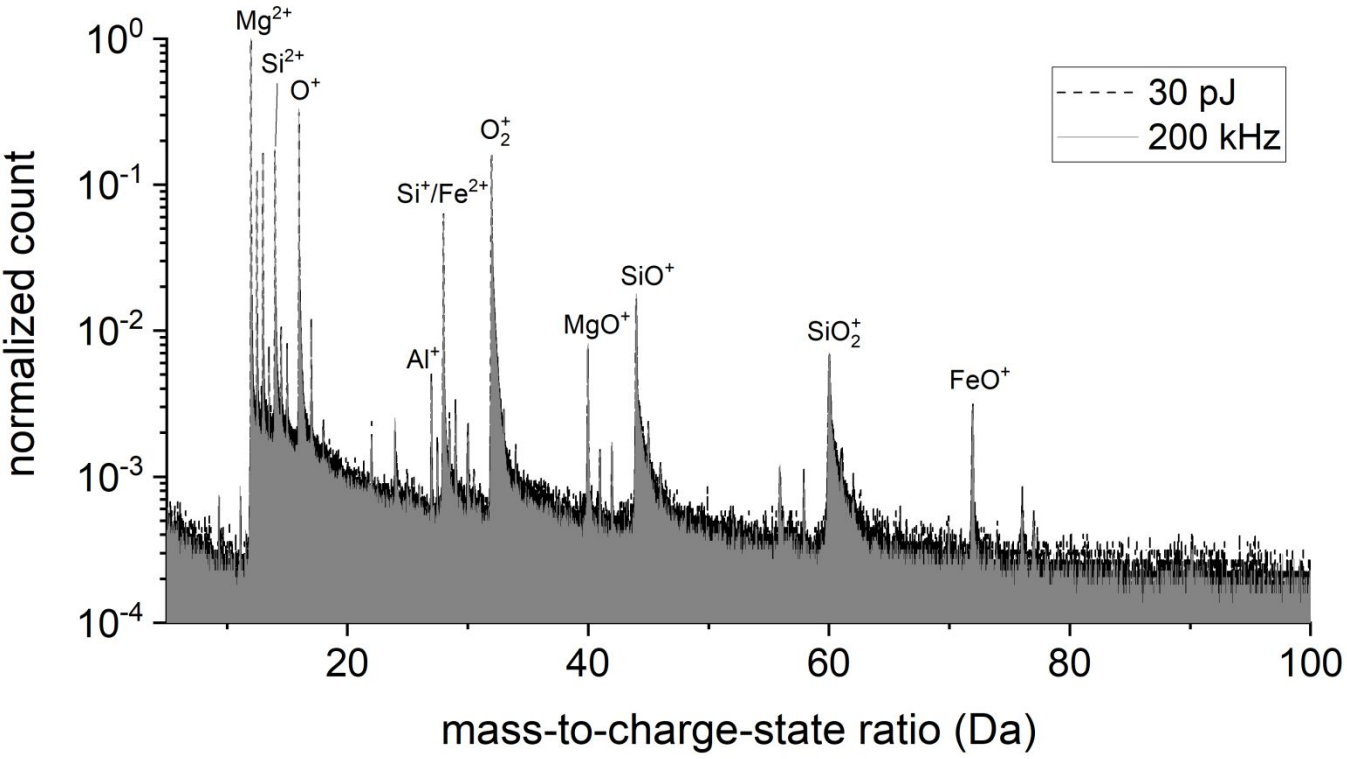

Figure SI3-5. Representative APT spectra of olivine (normalization to the highest peak)

Supplementary information

Testing the influence of laser pulse energy and rate in the atom probe tomography analysis of minerals

Chiara CAPPELLI[1,*] and Alberto PÉREZ-HUERTA[1]

[1]*Department of Geological Sciences, The University of Alabama, Tuscaloosa, AL 35487, USA*

*Corresponding author – E-mail: ccappelli@ua.edu

Supplementary 4.

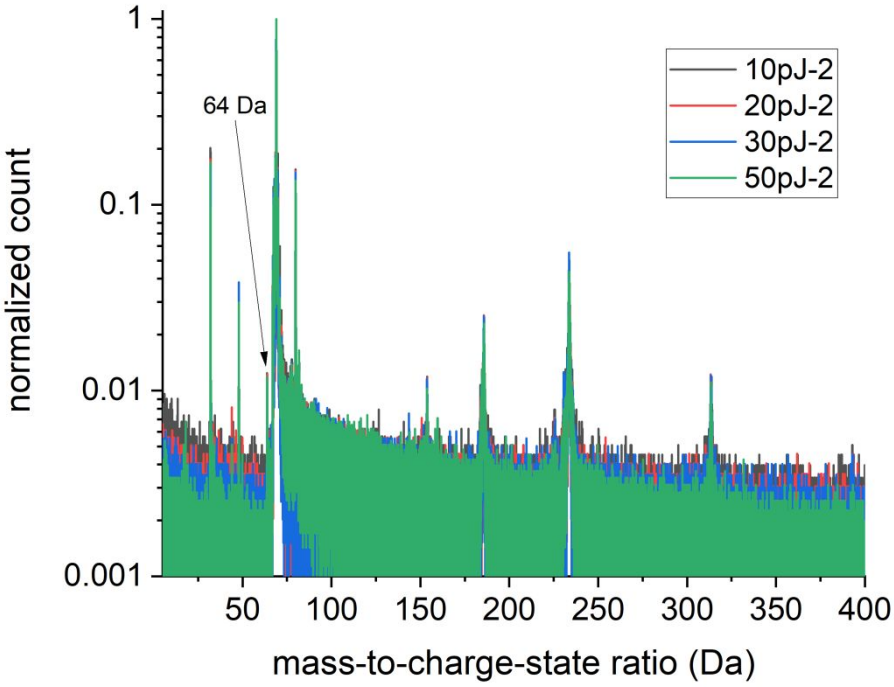

Figure SI4-1. Mass spectra of the PE testing of barite normalized to the maximum peak. The background varies between spectra and across the same spectrum (see main text for more details).

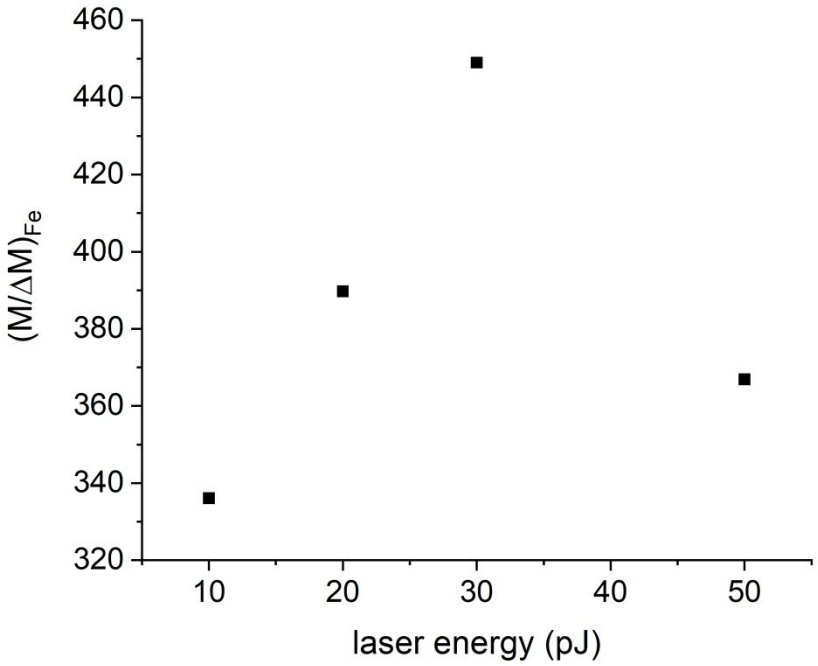

Figure SI4-2. Plot of the iron mass resolution, calculated by OriginPro-2020, as a function of the laser pulse energy. A maximum at 30 pJ is apparent.

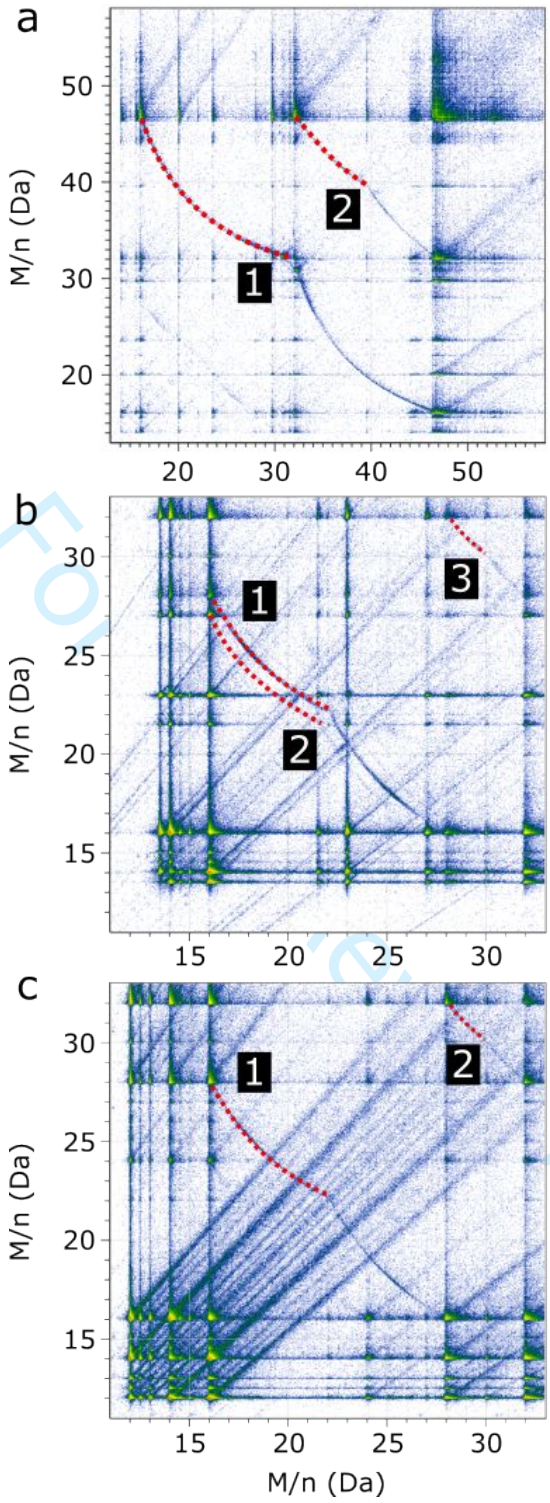

Figure SI4-3. Correlation histograms (Saxey plot) of selected ranges of mass-to-charge state ratio (M/n) of a) monazite (250 kHz run, PR testing), b) albite (30 pJ run, PE testing) and c) olivine (30 pJ run, PE testing). Horizontal, vertical and diagonal lines correspond to late evaporation events. Curve tracks correspond to dissociation of molecular species. The red lines and numbers indicates the estimated dissociation reactions (see main text).

Supplementary information

Testing the influence of laser pulse energy and rate in the atom probe tomography analysis of minerals

Chiara CAPPELLI[1,*] and Alberto PÉREZ-HUERTA[1]

[1]*Department of Geological Sciences, The University of Alabama, Tuscaloosa, AL 35487, USA*

*Corresponding author – E-mail: ccappelli@ua.edu

Supplementary 5.

The laser-specimen interactions and the atom evaporation from the surface of a sample immersed in a high electric field depend on the laser characteristic as well as the material properties and the specimen geometry (Bachhav et al., 2011; Cappelli et al., 2021b; Gault et al., 2010; Valderrama et al., 2015). Thermal conductivity (TC) and band gap (BG) are macroscopic properties that may define the behavior of a mineral during APT analysis (Table 1 in the main text). The plotting of the calculated baseline of all the studied minerals and conditions as a function of the thermal conductivity and laser pulse energy (Fig. SI5-1) and rate (Fig. SI5-2) reveals a good correlation suggesting that, to some extent, the background level depends on the heat transfer ability of the material. On the contrary, mass resolution does not seem to change with the thermal conductivity over the range of the obtained values. However, if As-pyrite, with much higher conductivity (and low band gap), is overlooked, a good correlation is found for the less conductive minerals.

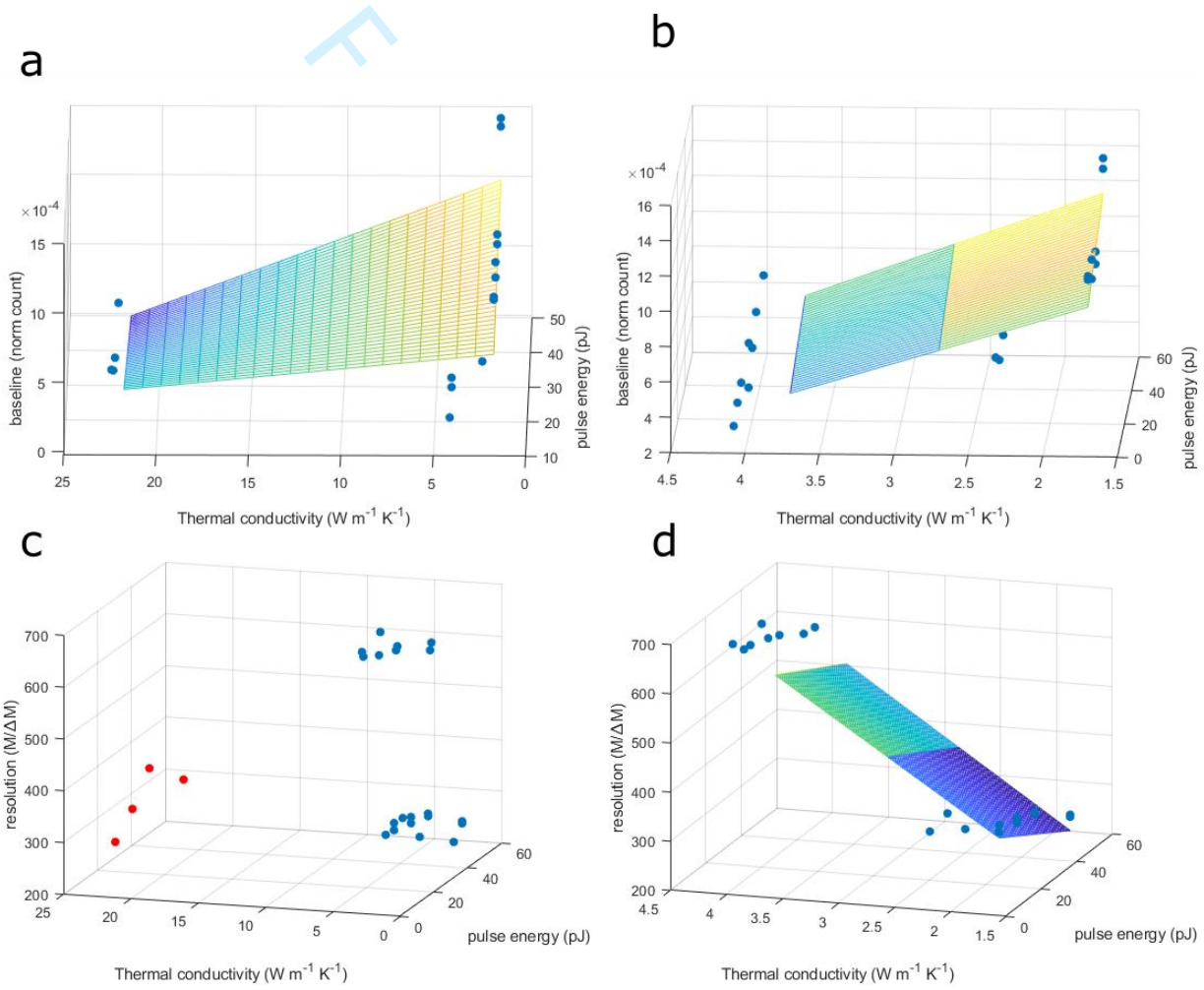

Figure SI5-1. Multivariable regression for baseline values (a,b) and mass resolution (c,d) as a function of thermal conductivity and laser pulse energy of the studied minerals for all the considered conditions. In b) and d) all data set except As-pyrite values. Red dots in (c) indicate As-pyrite data set.

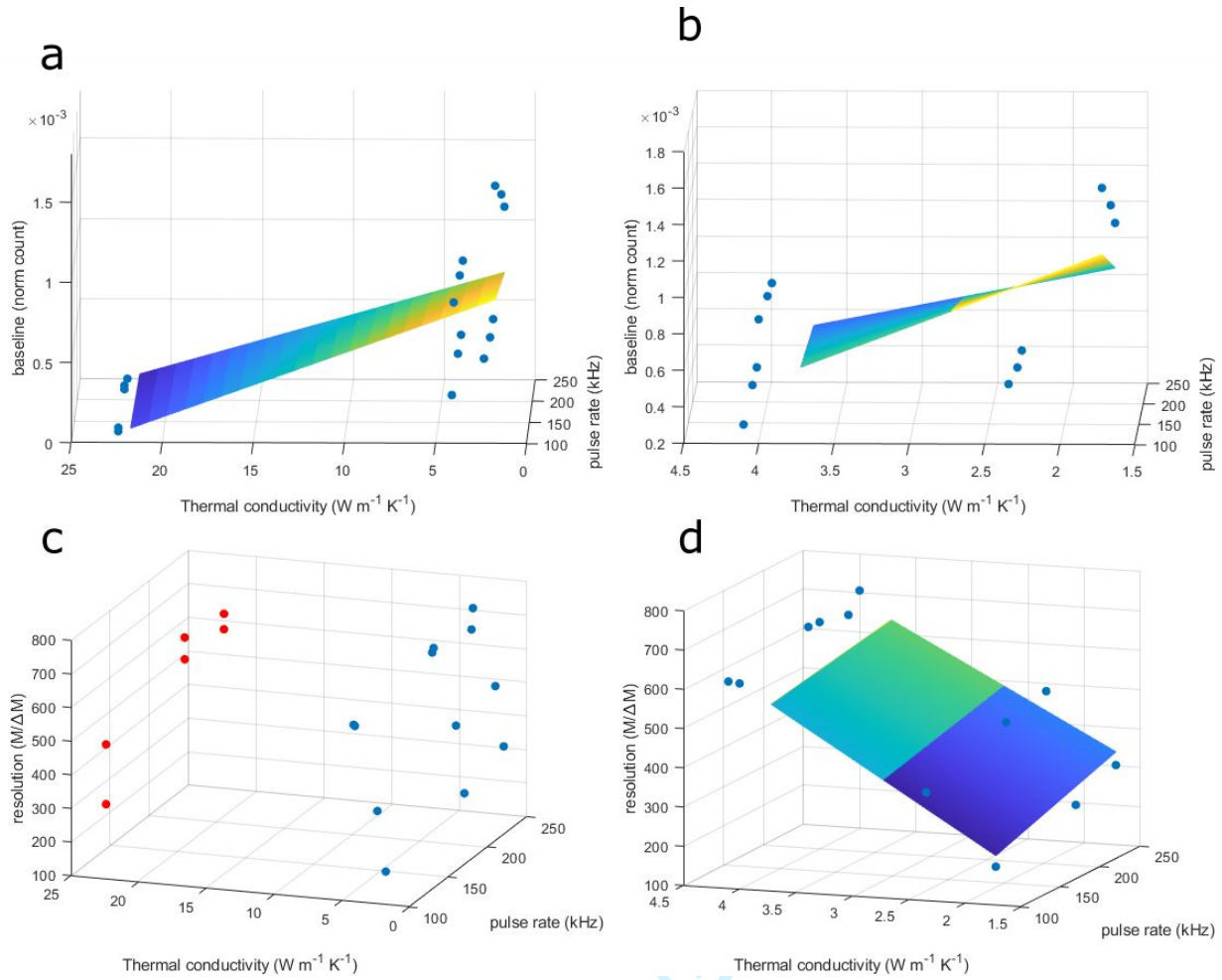

Figure SI5-2. Multivariable regression for baseline values (a,b) and mass resolution (c,d) as a function of thermal conductivity and laser pulse rate of the studied minerals for all the considered conditions. In b) and d) all data set except As-pyrite values. Red dots in (c) indicate As-pyrite data set. Note that the outlines in b) (Thermal conductivity 2.34 $Wm^{-1}K^{-1}$) correspond to the albite specimen, probably damage during the low kV FIB cleaning procedure (see main text for more details).

The multivariable regression of the output parameters and the band gap does not present good correlation. The lack of any relation between the BG and the quality parameters may be in fact related to the approximation of the mineral's band gap values. These values may greatly vary depending on the specific composition of the mineral. For example, the Fe content in olivine determine the specific band gap that can assume values as low as 3 eV (Cococcioni & de Gironcoli, 2005) in fayalite (iron end member). Hence for reliable considerations of the influence of this macroscopic property on the outcome of mineral APT analysis, exact values of the BG for the specific studied minerals should be available.